Dependence of X_CO on metallicity, intensity, and spatial scale in a self-regulated interstellar medium

Hu, C.-Y.; Schruba, A.; Sternberg, A.; Dishoeck, E.F. van

Citation

Hu, C. -Y., Schruba, A., Sternberg, A., & Dishoeck, E. F. van. (2022). Dependence of X_CO on metallicity, intensity, and spatial scale in a self-regulated interstellar medium. *The Astrophysical Journal*, *931*(1). doi:10.3847/1538-4357/ac65fd

The Astrophysical Journal, 931:28 (21pp), 2022 May 20 https://doi.org/10.3847/1538-4357/ac65fd

Dependence of $X_{\rm CO}$ on Metallicity, Intensity, and Spatial Scale in a Self-regulated Interstellar Medium

Chia-Yu Hu (胡家瑜)[1], Andreas Schruba[1], Amiel Sternberg[1,2,3], and Ewine F. van Dishoeck[1,4]
[1] Max-Planck-Institut für Extraterrestrische Physik, Giessenbachstrasse 1, D-85748 Garching, Germany; cyhu.astro@gmail.com
[2] School of Physics & Astronomy, Tel Aviv University, Ramat Aviv 69978, Israel
[3] Center for Computational Astrophysics, Flatiron Institute, 162 5th Avenue, New York, NY 10010, USA
[4] Leiden Observatory, Leiden University, P.O. Box 9513, NL-2300 RA Leiden, The Netherlands

Received 2022 January 11; revised 2022 April 1; accepted 2022 April 9; published 2022 May 20

Abstract

We study the CO(1–0)-to-H_2 conversion factor ($X_{\rm CO}$) and the line ratio of CO(2–1)-to-CO(1–0) (R_{21}) across a wide range of metallicity ($0.1 \leqslant Z/Z_\odot \leqslant 3$) in high-resolution (∼0.2 pc) hydrodynamical simulations of a self-regulated multiphase interstellar medium. We construct synthetic CO emission maps via radiative transfer and systematically vary the *observational* beam size to quantify the scale dependence. We find that the kpc-scale $X_{\rm CO}$ can be overestimated at low Z if assuming steady-state chemistry or assuming that the star-forming gas is H_2 dominated. On parsec scales, $X_{\rm CO}$ varies by orders of magnitude from place to place, primarily driven by the transition from atomic carbon to CO. The parsec-scale $X_{\rm CO}$ drops to the Milky Way value of 2×10^{20} cm^{-2} (K km s^{-1})$^{-1}$ once dust shielding becomes effective, independent of Z. The CO lines become increasingly optically thin at lower Z, leading to a higher R_{21}. Most cloud area is filled by diffuse gas with high $X_{\rm CO}$ and low R_{21}, while most CO emission originates from dense gas with low $X_{\rm CO}$ and high R_{21}. Adopting a constant $X_{\rm CO}$ strongly over- (under-) estimates H_2 in dense (diffuse) gas. The line intensity negatively (positively) correlates with $X_{\rm CO}$ (R_{21}) as it is a proxy of column density (volume density). On large scales, $X_{\rm CO}$ and R_{21} are dictated by beam averaging, and they are naturally biased toward values in dense gas. Our predicted $X_{\rm CO}$ is a multivariate function of Z, line intensity, and beam size, which can be used to more accurately infer the H_2 mass.

Unified Astronomy Thesaurus concepts: Interstellar medium (847); Astrochemistry (75); Hydrodynamical simulations (767)

1. Introduction

Molecular clouds are the site for star formation. Characterizing how they form from, and interact with, the diffuse interstellar medium (ISM) is crucial for our understanding of galaxy evolution (Lada & Lada 2003; McKee & Ostriker 2007; Tacconi et al. 2020). However, molecular hydrogen (H_2), the main component of molecular clouds, does not emit radiation under typical conditions. In contrast, carbon monoxide (CO), the second most abundant molecular species, is a very efficient emitter at low temperatures and therefore is the most commonly used tracer for H_2. The CO-to-H_2 conversion factor

$$X_{\rm CO} \equiv \frac{N_{\rm H_2}}{W_{10}}, \quad (1)$$

is used to convert the observed intensity of the CO(1–0) line intensity (W_{10}) to the H_2 column density ($N_{\rm H_2}$). The typical value found in the Milky Way is

$$X_{\rm CO,MW} = 2 \times 10^{20}\ {\rm cm^{-2}\ (K\ km\ s^{-1})^{-1}} \quad (2)$$

within ±30% uncertainty (see Bolatto et al. 2013 for a detailed review).

However, CO is not a perfect tracer for H_2. Even at solar metallicity, CO is photodissociated deeper into the cloud by the far-ultraviolet (FUV) radiation compared to H_2 (van Dishoeck & Black 1988; Sternberg & Dalgarno 1995), leading to a regime where H_2 gas is deficient in CO, commonly referred to as the *CO-dark* molecular gas (Wolfire et al. 2010). Furthermore, at low metallicities, the FUV radiation progressively photodissociates more CO but only mildly so the H_2 (Madden et al. 1997; Pak et al. 1998; Bolatto et al. 1999; Wolfire et al. 2010), which expands the range of column densities where gas is CO dark and leads to a higher $X_{\rm CO}$, making CO a poor tracer of H_2. Indeed, observations of nearby low-metallicity dwarf galaxies have found that the CO emission is extremely weak (often undetectable), and the ratio of the total star formation rate (SFR) to the CO luminosity is much higher than what is found in typical spiral galaxies (Schruba et al. 2012; Cormier et al. 2014). If we assume that the ratio of total SFR to H_2 mass is insensitive to metallicity, this implies an elevated $X_{\rm CO}$ at low metallicities. Therefore, theoretical expectations and observations both suggest that $X_{\rm CO}$ increases at lower metallicity.

Observational measurements of $X_{\rm CO}$ are challenging as they require not only a successful CO detection (which is difficult at low metallicities) but also an independent method to derive the H_2 mass. The existing techniques include the following: (1) The inverse Kennicutt–Schmidt (KS) method (Genzel et al. 2012; Schruba et al. 2012; Hunt et al. 2015; Amorín et al. 2016) measures the SFR, which is converted to the associated H_2 mass via an adopted correlation between the two quantities (i.e., the KS relation). (2) The dust-based method (Leroy et al. 2011; Elmegreen et al. 2013; Lee et al. 2015; Shi et al. 2015; Schruba et al. 2017) uses infrared (IR) continuum measurements to derive the dust mass, which is converted to the total gas mass with an assumed dust-to-gas ratio (DGR). The H_2 mass is then derived by subtracting the atomic hydrogen (H I) mass (obtained through 21 cm emission) from the total gas mass. (3) The virial method

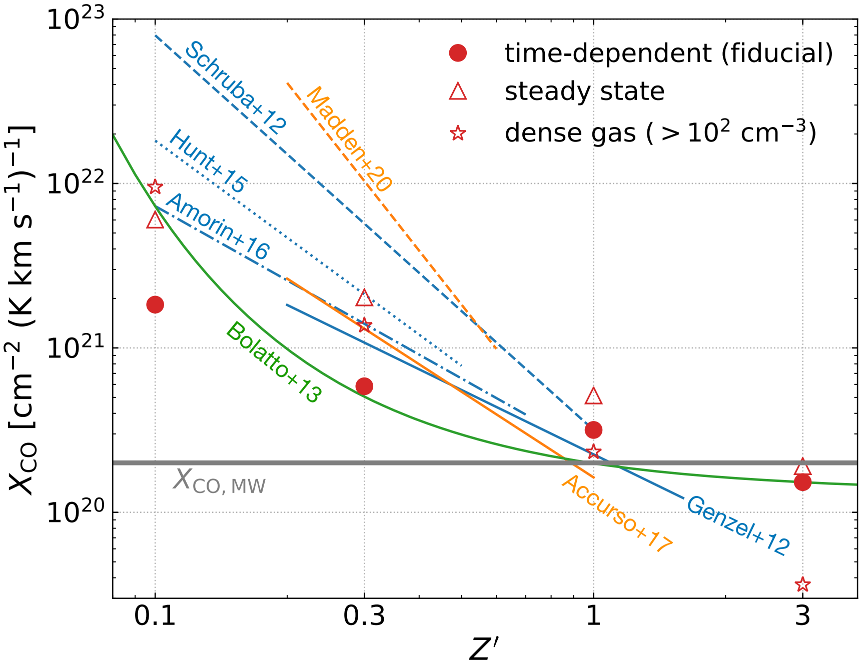

Figure 1. CO-to-H_2 conversion factor (X_{CO}) as a function of normalized metallicity ($Z' \equiv Z/Z_\odot$). The colored lines are from different observational studies as follows (showing only the dynamical range of Z' in each observation): Genzel et al. (2012), high-redshift ($z > 1$) star-forming galaxies (inverse KS method); Schruba et al. (2012), dwarf galaxies (inverse KS method); Hunt et al. (2015), dwarf galaxies (inverse KS method); Amorín et al. (2016), blue compact dwarf galaxies (inverse KS method); Accurso et al. (2017), local star-forming galaxies (spectral synthesis method); and Madden et al. (2020), dwarf galaxies (spectral synthesis method). The green solid curve shows the theoretical prescription from Bolatto et al. (2013). The horizontal gray line shows the standard Milky Way value (see Equation (2)). The red symbols show the time-averaged global (1 kpc^2) X_{CO} in our simulations (see Section 3.1). (Red-filled circles) our fiducial, time-dependent model; (red non-filled triangles) the steady-state model; and (red non-filled stars) the *dense gas* conversion factor $X_{100} \equiv N_H(n > 100\ \mathrm{cm^{-3}})/W_{10}$. Our time-dependent model can be described by Equation (8). At low Z', X_{CO} can be overestimated both by the spectral synthesis method (by assuming steady-state chemistry) and by the inverse KS method (by assuming the star-forming gas is fully molecular).

(Bolatto et al. 2008; Rubio et al. 2015; Schruba et al. 2017) measures the CO line width and the cloud size to derive the H_2 mass assuming that clouds are in virial equilibrium. (4) The spectral synthesis method (Accurso et al. 2017; Madden et al. 2020) measures the fine structure *metal* lines (e.g., [C II] 158 μm) in addition to the CO(1–0) line, and uses chemistry and spectral synthesis codes with assumed cloud geometry to constrain the physical parameters of the ISM and derive the H_2 mass. Each of these methods relies on different assumptions that are mostly calibrated at solar metallicity, and their validity at low metallicities remains unclear. Therefore, it is perhaps not too surprising that there are still significant discrepancies on the Z–X_{CO} relation derived from different observations (see Figure 1). On the other hand, the discrepancies may also indicate secondary dependencies. For example, the Z–X_{CO} relation appears to be steeper in dwarf galaxies than in more massive, star-forming galaxies in Figure 1.

Recently, high-resolution observations with the Atacama Large Millimeter/submillimeter Array (ALMA) have successfully detected CO at $Z' \equiv Z/Z_\odot \sim 0.1$ and shown that CO typically originates from compact regions of a few parsecs (Rubio et al. 2015; Shi et al. 2015; Schruba et al. 2017). More importantly, the X_{CO} derived from the virial method is found to be comparable to the Milky Way value and is significantly lower than the X_{CO} of the same targets derived from the dust-based method. This suggests a dependence on spatial scale (i.e., the beam size) as the high-resolution virial method measures X_{CO} in the compact (parsec-scale), CO-bright cores while the dust-based method, which typically has a much larger beam size ($\gtrsim$100 pc), measures X_{CO} averaging over entire molecular clouds (or associations), including both CO-bright and CO-dark gas. However, the fundamental small-scale distribution of X_{CO}, which dictates X_{CO} on different (larger) scales, is still poorly understood. The main goal of this paper is to shed light on this subject in a systematic way.

Meanwhile, the CO(2–1) line has become more widely used as an alternative to CO(1–0) in recent years. For example, the recent high-resolution survey of nearby star-forming galaxies, PHANGS-ALMA (Leroy et al. 2021), chose CO(2–1) over CO(1–0) for better sensitivity. In this case, inferring H_2 requires a two-step process: the observed CO(2–1) line intensity (W_{21}) is first converted into W_{10} with an adopted line ratio

$$R_{21} \equiv \frac{W_{21}}{W_{10}}, \tag{3}$$

and then converted into N_{H_2} with an adopted X_{CO}. Understanding how R_{21} varies with ISM properties is therefore important for CO(2–1) to be used as an alternative H_2 tracer (den Brok et al. 2021). Ultimately, for high-redshift galaxies, a similar method may be needed for CO lines of higher rotational levels.

Hydrodynamical simulations have been the theoretical frontiers of forward modeling the ISM structure, chemistry, and the observed line intensities. However, earlier studies have fundamental limitations in their setup. On small scales, cloud simulations (e.g., Glover & Mac Low 2011; Shetty et al. 2011a, 2011b; Glover & Clark 2012a; Bisbas et al. 2017, 2021; Peñaloza et al. 2017, 2018) provide detailed information with very high resolution ($\lesssim$0.1 pc) but rely on unrealistic boundary conditions (e.g., isolated clouds) and artificial forces for turbulence driving. In addition, they do not provide information on the ISM on kiloparsec scales that is typical for extragalactic observations. On the other hand, large-scale galaxy simulations with resolution $\gtrsim$50 pc (e.g., Feldmann et al. 2012; Narayanan et al. 2012) cannot resolve the structures of molecular clouds and therefore rely on oversimplified assumptions on the subgrid gas distribution. Significantly better resolutions have been achieved in isolated Milky Way–like galaxy simulations (Duarte-Cabral et al. 2015; Richings & Schaye 2016), but they were still insufficient to properly resolve the ISM.

Recently, it has become feasible to simulate a kiloparsec-scale ISM patch and follow star formation and stellar feedback self-consistently, establishing a more realistic, self-regulated system with parsec-scale resolution such that the ISM structure and stellar feedback are resolved without resorting to sub-grid models (Gatto et al. 2017; Seifried et al. 2017, 2020; Gong et al. 2018; Smith et al. 2020). However, most of these studies focus on solar-metallicity, solar-neighborhood conditions, and the only exception (Gong et al. 2020) studied $X_{\rm CO}$ with a limited range of $0.5 \leqslant Z' \leqslant 2$, which still does not cover the *low-metallicity* regime.

In Hu et al. (2021) (hereafter HSvD21), we presented a suite of hydrodynamical simulations of a (1 kpc)^2 ISM patch with an unprecedented dynamical range spatially and temporally, running for 500 Myr and reaching sub-parsec ($\sim$0.2 pc) spatial resolution (which has previously only been achieved with the *zoom-in* techniques and was limited to a few megayears, e.g., Seifried et al. 2020; Smith et al. 2020). The long simulation time leads to a large sample of clouds at different evolutionary stages, while the sub-parsec resolution is crucial for resolving the compact CO-bright cores at low metallicities. Furthermore, the simulations cover a wide range of metallicities ($0.1 \leqslant Z' \leqslant 3$), probing the low-metallicity regime for the first time. The numerical framework self-consistently includes gravity, hydrodynamics, time-dependent cooling and H_2 chemistry, radiation shielding, individual star formation, and stellar feedback from supernovae and photoionization. To simultaneously resolve the ISM and model the chemistry accurately, a hybrid approach is introduced where H_2 is followed on the fly while the other chemical species, including CO, are modeled in post-processing by a more detailed network.

In this paper, we construct synthetic emission maps of CO(1–0) and CO(2–1) from the simulations in HSvD21 with radiative transfer calculations. Our goal is to investigate the distributions of $X_{\rm CO}$ and R_{21} from parsec to kiloparsec scales at different metallicities and how they affect $X_{\rm CO}$ and R_{21} on systematically larger scales. Our paper is organized as follows. Section 2 describes our numerical setup for the radiative transfer calculation on an adaptive mesh. Section 3 is an overview of our simulation results, including our global $X_{\rm CO}$ compared against observations. Section 4 is a detailed analysis on the small-scale properties of CO excitation and optical depth. Section 5 shows our predicted $X_{\rm CO}$ and R_{21} on different spatial scales where we systematically increase the beam size from 2 pc to 1 kpc. Section 6 summarizes our work.

2. Numerical Methods

2.1. Simulations

Our simulations are presented in detail in HSvD21, which we briefly summarize as follows. The setup is an ISM patch with conditions similar to the solar neighborhood. The box size is 1 kpc along the x- and y-axes with periodic boundary conditions and 10 kpc along the z-axis with outflow boundary conditions. The origin is defined at the box center and $z = 0$ represents the midplane of the disk. The simulations were conducted using the public version of Gizmo (Hopkins 2015), a multi-solver code featuring the meshless Godunov method (Gaburov & Nitadori 2011) built on the TreeSPH code Gadget-3 (Springel 2005). Gravity is solved by the *treecode* method (Barnes & Hut 1986) while hydrodynamics are solved by the meshless finite-mass (MFM) method (Hopkins 2015). Time-dependent cooling and H_2 chemistry are included based on Glover & Mac Low (2007) and Glover & Clark (2012b), with a HEALPIX (Górski & Hivon 2011)-based treatment for radiation shielding similar to Clark et al. (2012). Star formation is based on the commonly used, stochastic *Schmidt law* recipe with a star formation efficiency of 50%. The stellar masses are stochastically sampled from the stellar initial mass function of Kroupa (2001), which determine the lifetime of massive stars (Ekström et al. 2012) and the luminosity of ionizing radiation (Lejeune et al. 1997, 1998). Supernova feedback is purely thermal. Photoionization follows the method of Hu et al. (2017) that can properly account for overlapping H II regions. The FUV radiation field and cosmic-ray ionization rate are both spatially uniform but time dependent, scaled linearly with the total SFR. The metallicity is assumed to be constant both spatially and temporally.

Four simulations are run with metallicities of $Z' = 3,\ 1,\ 0.3,$ and 0.1. The dust-to-gas mass ratio is 1% at $Z' = 1$ and scales linearly with Z'. We first run the $Z' = 1$ model with an artificially less efficient feedback model for 100 Myr in order to mitigate the initial transient phase that tends to blow out the gaseous disk. This generates a multiphase ISM, which is then used by each simulation as the initial conditions. Each simulation is run for 500 Myr. The mass resolution is 1 $M_\odot$ per gas particle, which corresponds to $\sim$0.2 pc spatial resolution where the Jeans mass is resolved. The results are further post-processed with a more detailed chemistry network that includes CO chemistry, using the time-dependent H_2 abundances from the simulations. We assume that an external FUV radiation background (calculated from the SFR) is attenuated by the effects of dust shielding, H_2 self-shielding, and CO self- and mutual-shielding. The column densities of dust, H_2, and CO relevant for shielding are calculated using a pixel-based approach integrated up to a radius of 100 pc for each gas cell. The photodissociation rate coefficients and attenuation coefficients are taken from Heays et al. (2017).[5] The time-averaged SFR in all runs are close to the observed value in the solar neighborhood of $\Sigma_{\rm SFR,0} = 2.4 \times 10^{-3}\, M_\odot\,{\rm yr}^{-1}\,{\rm kpc}^{-2}$ (Fuchs 2009) within a factor of 50%. Therefore, the corresponding time-averaged FUV radiation field is close to the Draine field (Draine 1978) and the cosmic-ray ionization rate is close to $\zeta_{\rm CR} = 10^{-16}\,{\rm s}^{-1}$ (Indriolo & McCall 2012; Indriolo et al. 2015) in all runs.

2.2. Radiative Transfer on an Adaptive Mesh

We post-process our simulations with the publicly available radiative transfer code RADMC-3D (Dullemond et al. 2012) to generate the synthetic CO(1–0) and CO(2–1) emission maps in the face-on view. We describe the details as follows.

---

[5] https://home.strw.leidenuniv.nl/~ewine/photo/index.html

Before we perform radiative transfer, we first need to convert the particle-based gas properties in our simulations onto a mesh where RADMC-3D calculates the level population and the subsequent radiative transfer. Our simulations resolve the Jeans mass of the gas down to ~0.2 pc, which defines the smallest spatial scale. However, if we were to generate a uniform Cartesian mesh that covers the entire simulation domain with a spatial resolution of 0.2 pc, it would take 5000^3 cells, which is computationally infeasible both in terms of computing time and memory. In addition, a large fraction of the simulation domain is filled with CO-free diffuse gas, making a uniform mesh extremely computationally inefficient. As such, it is highly desirable to adopt an adaptive mesh where the finest cells are only employed in regions of dense molecular gas.

We generate an adaptive mesh by first building an octree where each leaf contains at most one gas particle. The root node of the octree is centered at $x = 0.5$ kpc, $y = 0.5$ kpc, and $z = 0$, with a size of 1 kpc on each side, which contains the vast majority of the gas.[6] This octree not only defines an adaptive mesh where the resolution improves (i.e., cell size decreases) with increasing gas density but also serves as a neighbor finder for interpolation (see below). As the smallest physically meaningful scale in our simulations is around 0.2 pc, we trim the mesh such that the size of the smallest cell is $h_{\min} = 1/2^{13}$ kpc $= 0.12$ pc (i.e., the maximum refinement level is 13). The mesh is then further refined to fulfill the *2:1 balance*, which avoids a sudden jump of refinement levels and optimizes the calculation of velocity gradients in RADMC-3D.

Once the adaptive mesh is generated, we interpolate the particle information onto the mesh with a scheme similar to the MFM method. For any scalar field A, the interpolated value at each cell center x_c is

$$\bar{A}(x_c) = \frac{\sum_j A_j K(|x_j - x_c|, h_j)}{\sum_j K(|x_j - x_c|, h_j)}, \tag{4}$$

where x_j and h_j are the location and smoothing length of particle j, respectively, $K(|x_j - x_c|, h_j) = \omega(|x_j - x_c|/h_j)/h_j^3$, and ω is the cubic spline kernel function. The summation is over all particles whose kernel overlaps x_c (i.e., $|x_j - x_c| \leqslant h_j$), which is done by a *scatter*-neighbor search on x_c using the particle octree. We find that this interpolation scheme is significantly more accurate than the conventional smoothed-particle hydrodynamics (SPH) scheme especially for the gas temperature. The effect of different interpolation schemes is discussed in Appendix D. We interpolate the following quantities onto the adaptive mesh: CO number density ($n_{\rm CO}$), H_2 number density ($n_{\rm H_2}$), gas temperature (T), velocity (v), and velocity dispersion[7] (σ_v).

We use the large-velocity gradient approximation module implemented by Shetty et al. (2011a) in RADMC-3D to account for radiation trapping and calculate the level population at each cell. The molecular data are taken from the Leiden Atomic and Molecular database (Schöier et al. 2005). The collision partner of CO is H_2 with an ortho-to-para ratio of 3, and the collisional rate coefficients are taken from Flower (2001) and Wernli et al. (2006).

The local line profile follows a Gaussian function

$$\phi(\nu) = \lambda_0/(\sqrt{\pi} b) e^{-\Delta v^2/b^2}, \tag{5}$$

where ν is the photon frequency, $\lambda_0 \equiv c/\nu_0$ (c is the speed of light and ν_0 is the line-center photon frequency), and $\Delta v \equiv c(\nu - \nu_0)/\nu_0$ is the Doppler velocity offset. The Doppler parameter $b \equiv \sqrt{2k_{\rm B}T/(\mu m_{\rm p}) + \sigma_v^2}$ accounts for both thermal and microturbulent line broadening, where $k_{\rm B}$ is the Boltzmann constant, $m_{\rm p}$ is the proton mass, and μ is the mean molecular weight.

Once the level populations are known, RADMC-3D solves the equation of radiative transfer along the z-axis through the adaptive mesh. For each simulation snapshot, we adopt 512×512 pixels (or rays) that cover the entire simulation domain of 1×1 kpc. This means a pixel size of $1000/512 \approx 2$ pc, which is 16 times coarser than our finest cell. It might therefore seem concerning that a substantial fraction of small cells could be missed by the rays. Fortunately, RADMC-3D has the capability of *recursive sub-pixeling*, where a ray is split into 2-by-2 rays recursively (similar to a quadtree) whenever it passes through a cell smaller than the pixel size. As our pixels coincide with the octree's hierarchical structure, all cells, including those smaller than 2 pc, are guaranteed to be properly *visited* by the rays and so flux conservation is ensured. This is of crucial importance especially at low metallicities as CO typically concentrates in small dense cores.

At each pixel, RADMC-3D produces a spectrum, i.e., the specific intensity I_ν as a function of ν. It is convenient to convert I_ν into radiation temperature

$$T_{\rm R} \equiv \frac{\lambda_0^2}{2k_{\rm B}} I_\nu. \tag{6}$$

The line intensity is defined as the velocity-integrated radiation temperature

$$W \equiv \int T_{\rm R}\, dv, \tag{7}$$

which is in units of K km s^{-1}. The numerical integration is done with the Simpson's rule. The velocity coverage of the emission spectra we adopt is ±20 km s^{-1}, which is wide enough to cover the vertical motion of the gas. The velocity resolution is 0.4 km s^{-1}, which is sufficient considering the thermal broadening alone leads to $b \approx 1$ km s^{-1} for $T = 100$ K. An example of typical spectra is shown in Appendix C.

For each snapshot, we run RADMC-3D following the abovementioned approach and generate 512×512 spectra of both the CO(1–0) and CO(2–1) transitions as well as their corresponding maps of line intensity W_{10} and W_{21}. We also obtain the number density of CO in the rotational levels $J = 0$, 1, and 2 on the adaptive mesh, denoted as n_0, n_1, and n_2, respectively. We conduct the calculation for 41 snapshots from 100–500 Myr with a time interval of 10 Myr. Throughout the paper, all results we show are time averaged over 400 Myr, except for the snapshots in Figures 3 and 4.

3. Overview of Simulation Results

3.1. Global Average Quantities

As shown in HSvD21, due to the long timescale of H_2 formation on dust grains, the dynamical effect significantly reduces the H_2 abundances leading to a lower total H_2 mass

---

[6] Gas at high latitude ($z > 0.5$ kpc) is essentially CO-free and therefore can be excluded without affecting our results.

[7] We first calculate the particle-based σ_v as the velocity dispersion within the gas smoothing length and then interpolate it onto the mesh.

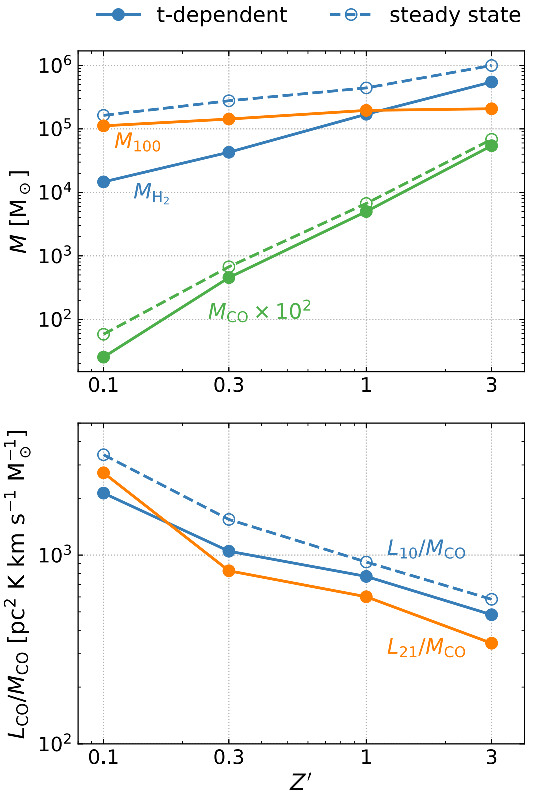

Figure 2. Upper panel: total mass of H_2 (blue), CO (green, multiplied by 100), and dense gas ($n > 100\ \mathrm{cm^{-3}}$, orange) as functions of Z'. Lower panel: luminosity-to-mass ratio of CO(1–0) (blue) and CO(2–1) (orange) as functions of Z'. The time-dependent and steady-state models are shown in solid and dashed lines, respectively.

(M_{H_2}) in the time-dependent model compared to its steady-state counterpart. In contrast, the effect on the CO abundance and thus the total CO mass (M_{CO}) is much weaker. This is demonstrated in the upper panel of Figure 2. In addition, M_{100} represents the total mass of the *dense gas*, which we define as $n > 100\ \mathrm{cm^{-3}}$, and it is nearly independent of Z', consistent with the fact that the average SFR in HSvD21 is insensitive to Z'. Compared to M_{H_2}, the star formation reservoir transitions from H_2 dominated at high Z' to H I dominated at low Z'.

While M_{H_2}, M_{CO}, and M_{100} are purely chemical and hydrodynamical properties, the CO luminosity-to-mass ratio (L_{CO}/M_{CO}, lower panel of Figure 2) is a result of radiative transfer. The luminosities of CO(1–0) and CO(2–1) are defined as $L_{10} = \int W_{10}\, da$ and $L_{21} = \int W_{21}\, da$, respectively, where the integration is over the $(1\ \mathrm{kpc})^2$ area. The luminosity-to-mass ratio is higher at low Z' mainly because the lines become increasingly optically thin, as will be discussed in Section 4.3.

The time-averaged global conversion factor is $X_{CO} = M_{H_2}/(2m_p L_{10})$ where m_p is the proton mass. We can now put these computed values in Figure 1 and compare them against observations. The red-filled circles and non-filled triangles represent our time-dependent model and steady-state model, respectively. The red non-filled stars show the *dense gas* conversion factor: $X_{100} \equiv N_H(n > 100\ \mathrm{cm^{-3}})/W_{10} = 0.71 M_{100}/(2m_p L_{10})$, where the factor 0.71 is the hydrogen mass fraction. Our fiducial time-dependent model can be fitted by (with a correlation coefficient of 0.99):

$$X_{CO} = 3.17\times10^{20} Z'^{-0.71}\ \mathrm{cm^{-2}\ (K\ km\ s^{-1})^{-1}}, \qquad (8)$$

which agrees well with the Milky Way value (Equation (2)) at $Z' = 1$ within 60%. The metallicity dependence is flatter compared to the steady-state counterpart where $X_{CO} \propto Z'^{-1}$. This is because the dynamical effect mainly suppresses H_2 formation but not CO formation. The dense gas conversion factor scales even more steeply as $X_{100} \propto Z'^{-1.5}$. This demonstrates that the dense, star-forming gas reservoir becomes H I dominated at low Z'. The implication is that X_{CO} at low Z' can be overestimated both by the spectral synthesis method (by assuming steady-state chemistry) and by the inverse KS method (by assuming the star-forming gas is fully molecular).

At super-solar metallicity ($Z' = 3$), our steady-state model agrees very well with our fiducial time-dependent model. Steady-state chemistry is a good approximation as the H_2 formation time is short. However, the dense gas conversion factor is significantly lower than X_{CO}, which reflects the fact that a large fraction of diffuse (and presumably cold) gas is molecular.

3.2. Visual Impression

Figure 3 shows face-on maps[8] of N_{H_2}, N_{CO}, W_{10}, and W_{21} from left to right with a beam size of $l_b = 2$ pc in the $Z' = 1$ run at $t = 420$ Myr (upper row) and the $Z' = 0.1$ run at $t = 130$ Myr (lower row). The entire simulation domain of $1\ \mathrm{kpc}^2$ is shown. Qualitatively, CO only exists in the inner part of the H_2 clouds where the gas is dense and well shielded. Both H_2 and CO are more compact in the $Z' = 0.1$ case. The distribution of W_{10} is very similar to that of N_{CO} except at the densest cores where W_{10} is slightly reduced compared to N_{CO}. This is because CO(1–0) transitions from the optically thin regime where $W_{10} \propto N_{CO}$ to the optically thick regime where W_{10} saturates. W_{21} follows a similar distribution to W_{10} but is less spatially extended, as the $J = 2$ level is not sufficiently excited in the diffuse gas.

However, for extragalactic observations, a parsec-scale resolution is often inaccessible. Therefore, we construct N_{H_2}, N_{CO}, W_{10}, and W_{21} at coarser beam sizes from our results for $l_b = 2$ pc. The beam size is systematically increased by factors of 2 up to $l_b = 1$ kpc, which includes the entire simulation domain. For example, N_{H_2} and W_{10} at $l_b = 4$ pc are constructed from the results at $l_b = 2$ pc:

$$N_{H_2}(4\ \mathrm{pc}) = \frac{\int N_{H_2}\, da}{\int da} = \frac{1}{2^2}\sum_{i=1}^{4} N_{H_2,i}(2\ \mathrm{pc}), \qquad (9)$$

$$W_{10}(4\ \mathrm{pc}) = \frac{\int W_{10}\, da}{\int da} = \frac{1}{2^2}\sum_{i=1}^{4} W_{10,i}(2\ \mathrm{pc}), \qquad (10)$$

where the integration is over the area of a 4 pc beam and the summation is over the 2-by-2 sub-beams of $l_b = 2$ pc, which constitute a 4 pc beam. Likewise, a 8 pc beam is constructed from the 4-by-4 sub-beams of 2 pc (or, equivalently, from the 2-by-2 sub-beams of 4 pc), and so forth.

---

[8] We note that HSvD21 distinguishes between the LOS integrated column density (N^{obs}) and the column density available for radiation shielding (N^{eff}). In this work, we refer by column density exclusively to N^{obs}.

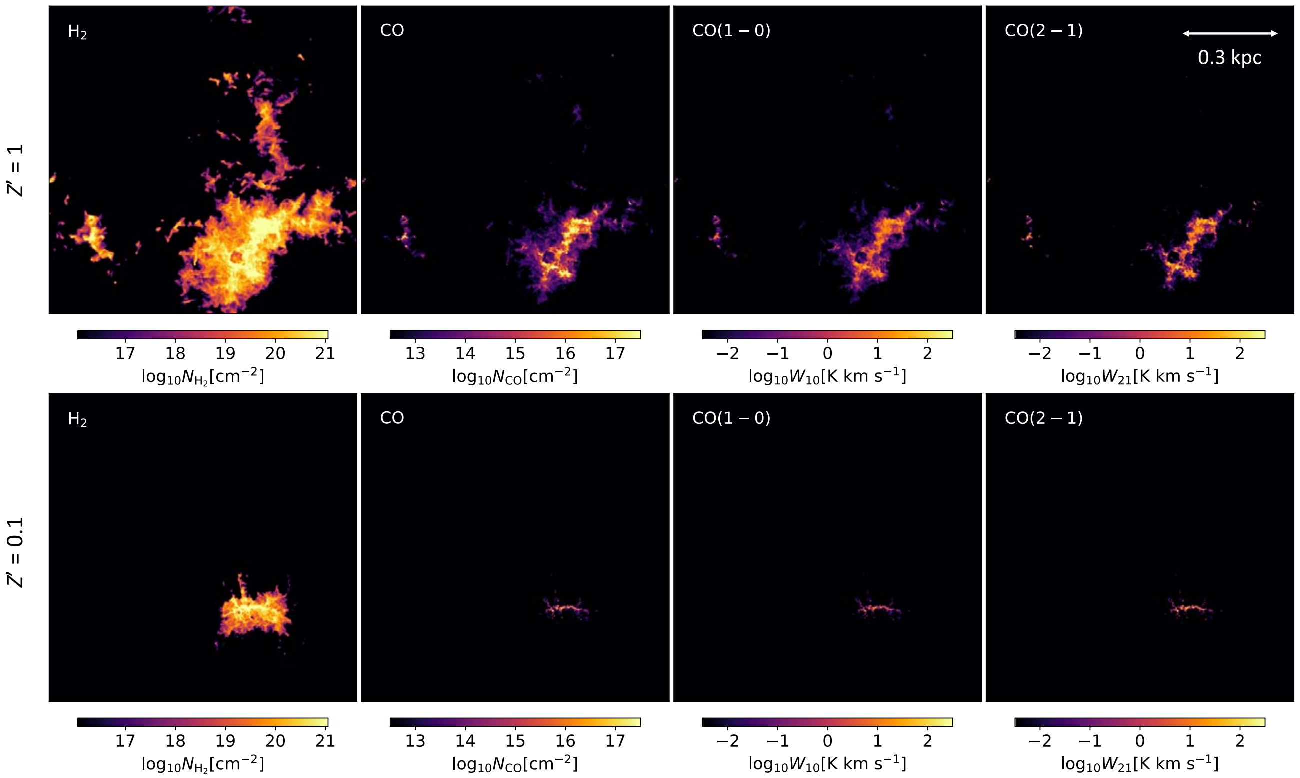

Figure 3. Face-on maps of H_2 column density, CO column density, CO(1–0) line intensity, and CO(2–1) line intensity from left to right in the solar-metallicity ($Z' = 1$) run at $t = 420$ Myr (upper row) and the $Z' = 0.1$ run at $t = 130$ Myr (lower row). The entire simulation domain of 1 kpc^2 is shown. H_2 is spatially more extended than CO. Both H_2 and CO are more compact at low metallicity.

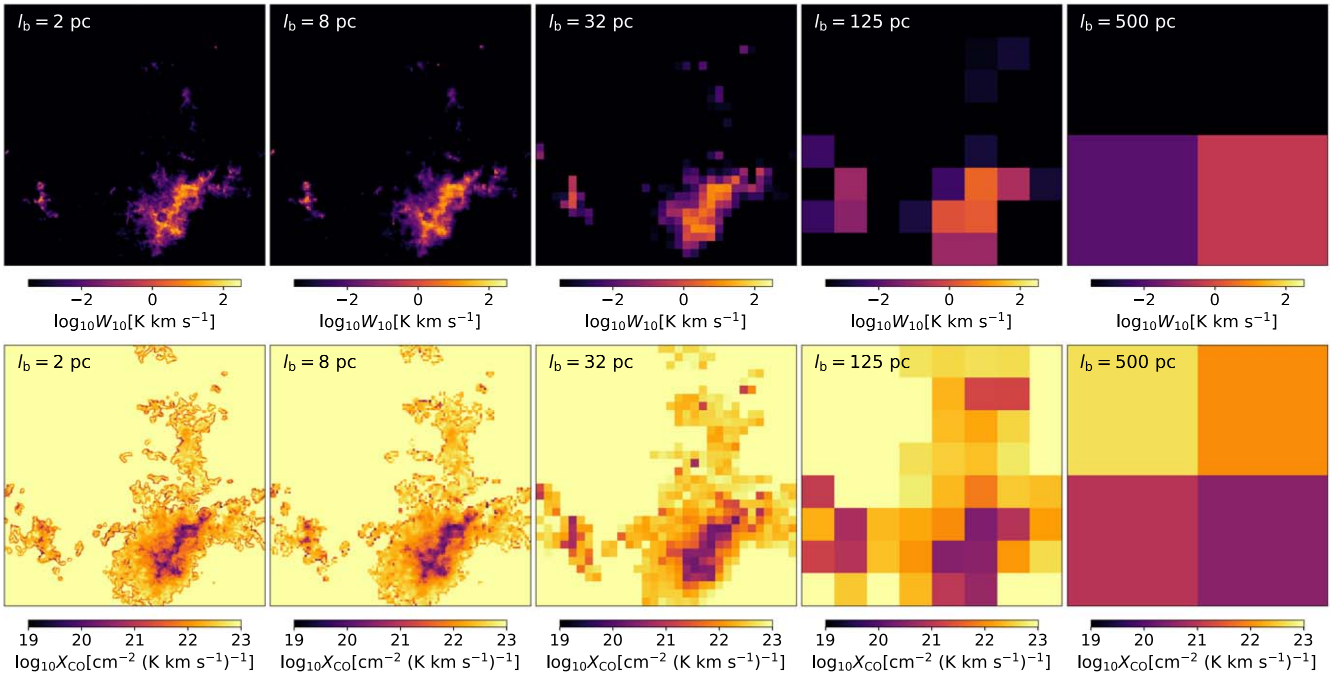

Figure 4. Face-on maps of W_{10} (upper row) and X_{CO} (lower row) with beam size $l_b = 2$, 8, 32, 125, and 500 pc from left to right. Note that the Milky Way X_{CO} factor (Equation (2)) is represented by the dark purple color.

To illustrate the effect of spatial averaging/smoothing, Figure 4 shows the maps of W_{10} (upper row) and X_{CO} (lower row) for $l_b = 2$, 8, 32, 125, and 500 pc from left to right. On the 2 pc scale, X_{CO} varies by orders of magnitude: it is low in the dense, well-shielded gas and high in the diffuse gas. We stress that our radiative transfer calculations are done with a much smaller minimal cell size ∼0.2 pc with the sub-pixeling technique (see Section 2.2). On large scales, as long as the beam contains dense gas (which only occupies a small area), the beam-averaged X_{CO} is driven toward low values (in purple).

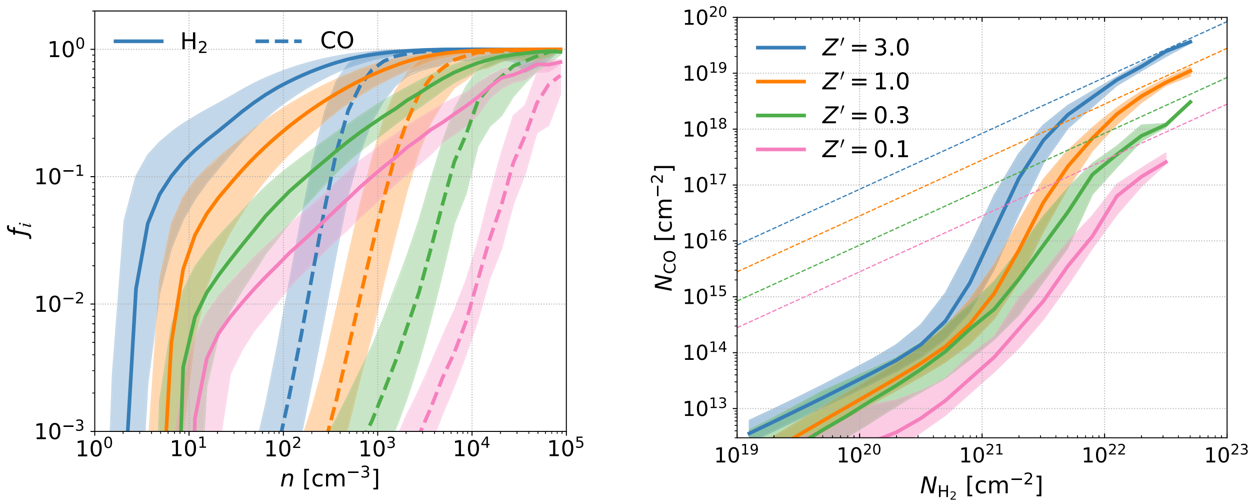

Figure 5. Left panel: normalized fractional abundance of H$_2$ (solid lines) and CO (dashed lines) as functions of hydrogen number density n for normalized metallicity $Z' = 3$, 1, 0.3, and 0.1. Right panel: H$_2$ column density vs. CO column density for $Z' = 3$, 1, 0.3, and 0.1. The thin dashed lines indicate the maximum ratio $N_{CO}/N_{H_2} = 2x_{C,0}$ where carbon is completely in form of CO. In both panels, the lines represent the median values while the shaded areas enclose the 25th and 75th percentiles.

This will be discussed more quantitatively in Section 5 after we provide more insight and background information on the simulations at the molecular level in Section 4.

3.3. Chemical Properties

In this section, we briefly describe the distributions of H$_2$ and CO in the simulations. Although these chemical properties have been shown in HSvD21, they are the basis of our radiative transfer and provide context for the results in Figure 4, so they are worth repeating here.

We define the number abundance of a chemical species i as $x_i \equiv n_i/n$, where n is the hydrogen number density and n_i is the number density of species i. The normalized fractional abundance of H$_2$ is then defined as $f_{H_2} \equiv 2x_{H_2}$ such that $f_{H_2} = 1$ when all hydrogen is in the form of H$_2$. Similarly, the normalized fractional abundance of CO is defined as $f_{CO} \equiv x_{CO}/x_{C,0}$, where $x_{C,0} = 1.4 \times 10^{-4} Z'$ is the total carbon abundance. The left panel of Figure 5 shows f_{H_2} (solid lines) and f_{CO} (dashed lines) as functions n. At a given Z', CO forms at higher densities than where H$_2$ forms, consistent with the visual impression in Figure 3. Both H$_2$ and CO exist at increasingly higher densities as Z' decreases due to the deficit of dust.

The right panel of Figure 5 shows N_{CO} as a function of N_{H_2}. The N_{H_2}–N_{CO} relation is characterized by three regimes: (i) the CO-poor regime at low N_{H_2} where the CO-to-H$_2$ ratio $\gamma \equiv N_{CO}/N_{H_2}$ is low; (ii) the transition regime at intermediate N_{H_2} where γ increases sharply with N_{H_2}, which reflects the formation of CO; and (iii) the CO-rich regime at high N_{H_2} where γ approaches its upper limit (indicated by the thin dashed lines).

4. Molecular Physics

In this section, we present a detailed analysis of the *microphysics* in our simulations and discuss how the lines are excited and propagated in the ISM, which forms the backbone of the observables. The readers interested only in our predicted X_{CO} and R_{21} may want to skip this section and go directly to Section 5.

4.1. CO Excitation

In the upper panel of Figure 6, we show the excitation temperature of CO(1–0) (T_{exc}, solid lines) and kinetic temperature (T_{kin}, dashed lines) as a function of n. In low-density gas where collisions are unimportant, T_{exc} is set by the background radiation $T_{bg} = 2.73$ K due to the cosmic microwave background (CMB). As n increases, T_{exc} gradually increases and approaches T_{kin}, and the line is *thermalized* when $T_{exc} = T_{kin}$. At the highest densities, T_{kin} (and therefore T_{exc}) is higher at low Z' due to heating from H$_2$ formation and UV pumping (Bialy & Sternberg 2019). Interestingly, CO(1–0) is thermalized at higher densities as Z' decreases. This is caused by a combination of two effects at low Z'. First, the collision partner H$_2$ forms at densities higher than the critical density of CO(1–0). Therefore, it takes a higher total hydrogen number density to thermalize the line. Second, higher CO abundance results in more efficient radiation trapping (more optically thick) and thus a lower effective critical density.

The CO population ratio (r_{21}) of level $J = 2$ to level $J = 1$ follows a similar trend. In the lower panels of Figure 6, we show r_{21} as a function of n (left) and n_{H_2} (right) in solid lines. Analytically, the population ratio of level J to level $J' = J - 1$ can be expressed as a function of T_{exc}:

$$r_{JJ'}(T_{exc}) = \frac{(2J + 1)e^{-B_0 J(J+1)/T_{exc}}}{(2J' + 1)e^{-B_0 J'(J'+1)/T_{exc}}} = \frac{g_J}{g_{J'}} e^{-T_{JJ'}/T_{exc}}, \tag{11}$$

where g_J and $g_{J'}$ are the degeneracy in level J and J', respectively, $B_0 = 2.77$ K, $T_{JJ'} = 2JB_0 = E_{JJ'}/k_B$, and $E_{JJ'}$ is the energy difference between levels J and J'. For $J = 2$ and $J' = 1$, it follows

$$r_{21}(T_{exc}) = \frac{5}{3} e^{-11.1\ \mathrm{K}/T_{exc}}. \tag{12}$$

Note that T_{exc} here is specifically for CO(2–1), which can be different from the excitation temperature of CO(1–0) unless the gas is in LTE. At low densities where $T_{exc} = 2.73$ K, our results agree well with the analytic expectation $r_{21}(2.73\ \mathrm{K}) = 0.029$.

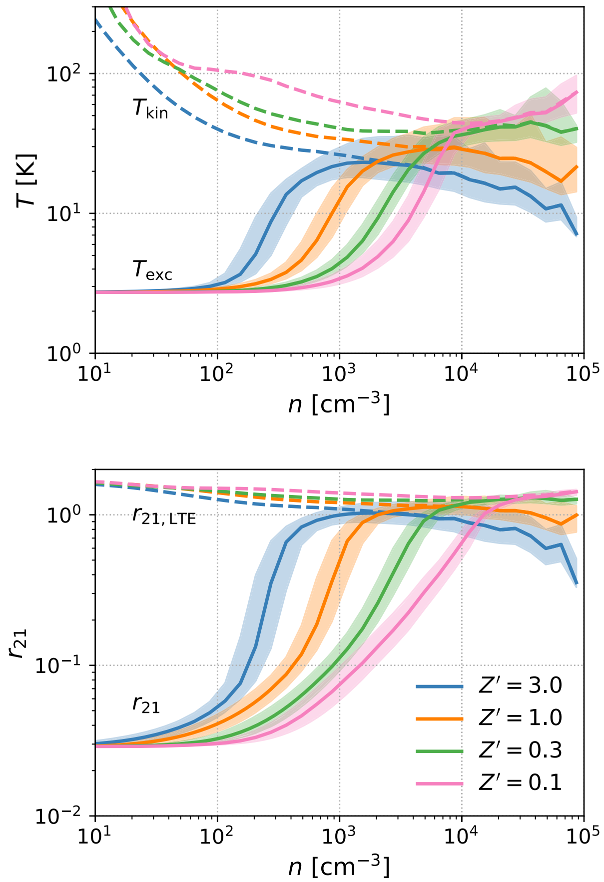

Figure 6. Upper panel: excitation temperature of CO(1–0) ($T_{\rm exc}$, solid lines) and kinetic temperature ($T_{\rm kin}$, dashed lines) as a function of n. Lower panel: CO population ratio of $J = 2$ to $J = 1$ (r_{21}, solid lines) as a function of n. The dashed lines show the CO population ratio assuming local thermodynamic equilibrium ($r_{21,\rm LTE}$). The lines represent the median values while the shaded areas enclose the 25th and 75th percentiles (not shown for $T_{\rm kin}$ and $r_{21,\rm LTE}$ for the sake of clarity). The lines thermalize at higher densities at low Z' as the collision partner H_2 forms at densities higher than the critical densities and the lower CO abundance leads to less efficient radiation trapping.

As n increases, r_{21} gradually increases and approaches the LTE line ratio $r_{21,\rm LTE}$ (dashed lines), which we obtain using Equation (12) assuming $T_{\rm exc} = T_{\rm kin}$. At $Z' \geqslant 1$, the decline of r_{21} at high n is due to the decline of $T_{\rm kin}$ instead of subthermal excitation. The maximum r_{21} is around unity at all metallicities and is slightly higher at low Z' due to higher $T_{\rm kin}$, though the effect is very mild. Indeed, Equation (12) suggests that r_{21} is not very sensitive to $T_{\rm exc}$ when $T_{\rm exc} \gg 11.1$ K and it asymptotes to an upper limit of $5/3 \approx 1.66$ as $T_{\rm exc} \to \infty$.

4.2. Optically Thin Limit

At low $N_{\rm CO}$, the lines are in the optically thin limit and self-absorption can be neglected. The emissivity of the CO(J–J') transition is

$$j_\nu = \frac{E_{JJ'}}{4\pi} n_J A_{JJ'} \phi(\nu), \tag{13}$$

where n_J is the number density of CO in level J and $A_{JJ'}$ is the Einstein coefficient for spontaneous decay. As there is no absorption, the specific intensity is simply $I_\nu = \int j_\nu\, dz$ and thus the line intensity can be written as

$$\begin{aligned} W_{JJ',\rm thin} &= \frac{\lambda_{JJ'}^2}{2k_{\rm B}} \iint j_\nu\, dz\, dv \\ &= \frac{\lambda_{JJ'}^3}{8\pi} T_{JJ'} A_{JJ'} \int n_{\rm CO} f_J\, dz, \end{aligned} \tag{14}$$

where $\lambda_{JJ'} = hc/E_{JJ'}$ is the line-center wavelength, h is the Planck constant, and $f_J \equiv n_J/n_{\rm CO}$ is the fraction of CO in level J. If we define the $n_{\rm CO}$-weighted line-of-sight (LOS) average f_J as

$$\overline{f_J} \equiv \frac{\int n_{\rm CO} f_J\, dz}{\int n_{\rm CO}\, dz} = \frac{N_{{\rm CO},J}}{N_{\rm CO}}, \tag{15}$$

where $N_{\rm CO}$ is the CO column density and $N_{{\rm CO},J}$ is the column density of CO in level J, we obtain

$$W_{JJ',\rm thin} = \frac{\lambda_{JJ'}^3}{8\pi} T_{JJ'} A_{JJ'} N_{\rm CO} \overline{f_J}. \tag{16}$$

Namely, $W_{JJ',\rm thin}$ scales linearly with $N_{\rm CO}$, with a secondary dependency on $\overline{f_J}$. Note that Equation (16) is independent of the line width b as expected for optically thin conditions.

Analytically, f_J can be expressed as a function of the excitation temperature $T_{\rm exc}$,

$$\begin{aligned} f_J\,(T_{\rm exc}) &= \frac{(2J+1)e^{-B_0 J(J+1)/T_{\rm exc}}}{\sum_J (2J+1)e^{-B_0 J(J+1)/T_{\rm exc}}} \\ &\approx \frac{(2J+1)e^{-B_0 J(J+1)/T_{\rm exc}}}{\sqrt{1+(T_{\rm exc}/B_0)^2}}, \end{aligned} \tag{17}$$

where the approximation of the partition function in the denominator is accurate to within ±6% for all $T_{\rm exc}$ (Draine 2011, Chapter 19). Adopting $A_{10} = 7.2 \times 10^{-8}$ s^{-1}, $A_{21} = 6.91 \times 10^{-7}$ s^{-1}, $T_{10} = 5.53$ K, $T_{21} = 11.1$ K, $\lambda_{10} = 0.26$ cm, and $\lambda_{21} = 0.13$ cm, the line intensities in the optically thin regime become

$$W_{10,\rm thin} = 7.82 \text{ K km s}^{-1} N_{\rm CO,16} \frac{\overline{f_1}}{f_1(2.73)}, \tag{18}$$

$$W_{21,\rm thin} = 0.54 \text{ K km s}^{-1} N_{\rm CO,16} \frac{\overline{f_2}}{f_2(2.73)}, \tag{19}$$

where $N_{\rm CO,16} \equiv N_{\rm CO}/(10^{16}\ {\rm cm}^{-2})$.

In the left panels in Figure 7, we show W_{10} (upper) and W_{21} (lower) as functions of $N_{\rm CO}$ at different Z'. At the lowest $N_{\rm CO}$ where collisional excitation is inefficient, $T_{\rm exc} = 2.73$ K and thus W_{10} and W_{21} follow the dashed lines, which indicate $W_{10} = 7.82 N_{\rm CO,16}$ K km s^{-1} and $W_{21} = 0.54 N_{\rm CO,16}$ K km s^{-1} in the upper and lower panels, respectively. For $N_{\rm CO} < 10^{16}$ cm^{-3}, W_{10} scales linearly with $N_{\rm CO}$ as the secondary factor $\overline{f_1}$ does not vary much with $N_{\rm CO}$. This is shown in the upper right panel of Figure 7. Since the $J = 1$ level is only 5.53 K above the ground state, it is already significantly excited by the CMB radiation alone ($f_1(2.73\ {\rm K}) = 0.28$). In contrast, W_{21} scales super-linearly with $N_{\rm CO}$ in the optically thin regime where $\overline{f_2}$ provides a secondary contribution. Indeed, $\overline{f_2}$ increases significantly with $N_{\rm CO}$, from $f_2(2.73\ {\rm K}) = 8.08 \times 10^{-3}$ to a maximum value of ∼0.3.

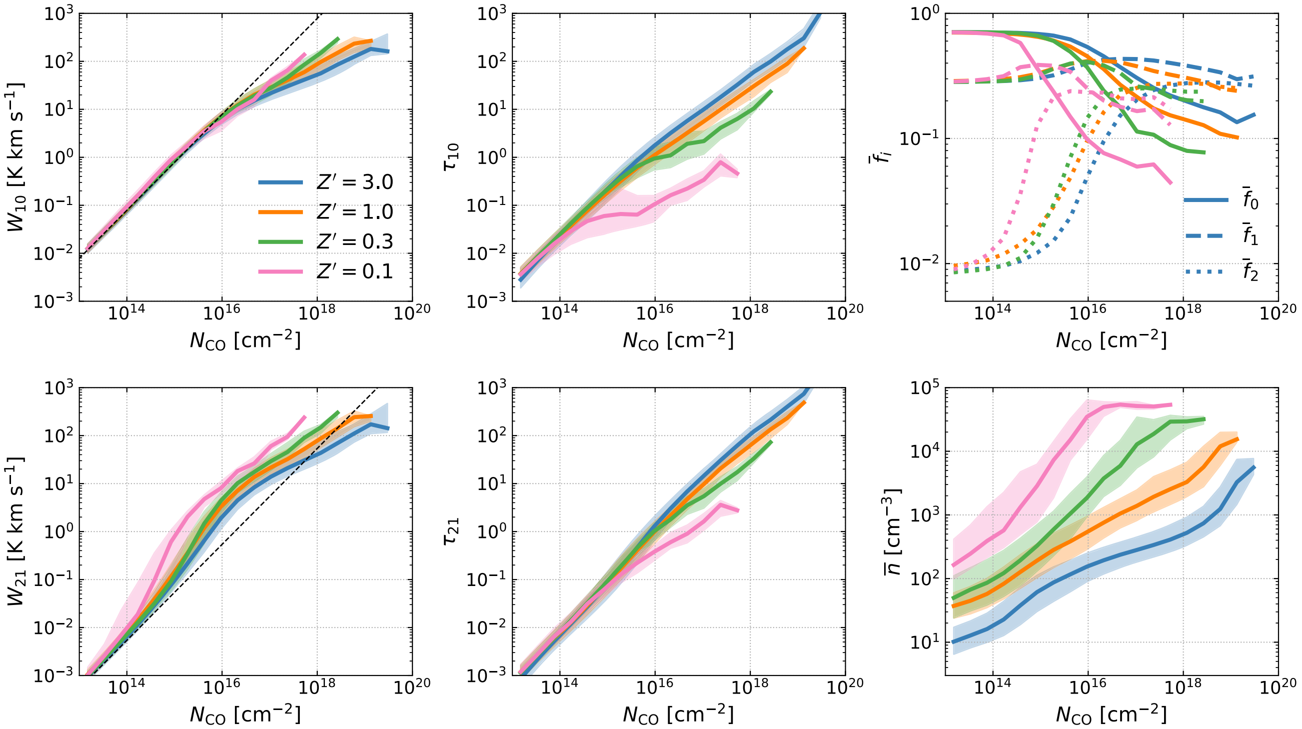

Figure 7. Left panels: line intensity of CO(1–0) (upper) and CO(2–1) (lower) as a function of N_{CO}. The dashed lines in the upper and lower panels indicate $W_{10,thin}/N_{CO,16} = 7.82$ K km s^{-1} and $W_{21,thin}/N_{CO,16} = 0.54$ K km s^{-1}, respectively. Middle panels: optical depth of CO(1–0) (upper) and CO(2–1) (lower) as a function of N_{CO}. Upper right panel: the n_{CO}-weighted average fraction of CO in the rotational level $J = 0$ (solid), 1 (dashed), and 2 (dotted) as functions of N_{CO}. Lower right panel: the n_{CO}-weighted average hydrogen number density as a function of N_{CO}. The lines represent the median values while the shaded areas enclose the 25th and 75th percentiles in all panels (not shown for $\overline{f_J}$ for the sake of clarity).

In addition, the excitation of both $J = 1$ and $J = 2$ occurs at lower N_{CO} as Z' decreases. Assuming a positive correlation between n and N_{CO}, this seems to be in conflict with Figure 6 where thermalization occurs at higher densities at low Z'. However, since CO only exists in the small and dense cores at low Z', the corresponding gas density is higher at a given N_{CO}. This is demonstrated in the lower right panel of Figure 7, where we show the n_{CO}-weighted LOS average hydrogen number density,

$$\bar{n} \equiv \frac{\int n_{CO} n \, dz}{\int n_{CO} \, dz}, \tag{20}$$

as a function of N_{CO}. Indeed, $\bar{n}$ correlates positively with N_{CO} at all Z'. However, at a given N_{CO}, $\bar{n}$ increases inversely with Z'. The net effect is that as Z' decreases the excitation of both $J = 1$ and $J = 2$ occurs at a lower N_{CO}.

4.3. Optical Depth Effect

The optical depth at the line center of CO(J–J') can be expressed as

$$\tau_{JJ'} = \frac{\lambda_{JJ'}^3 A_{JJ'} g_J}{8\pi^{3/2} g_{J'}} \int \frac{n_{J'}}{b} \left(1 - \frac{n_J g_{J'}}{n_{J'} g_J}\right) dz. \tag{21}$$

Adopting $g_0 = 1$, $g_1 = 3$, and $g_2 = 5$, we obtain

$$\tau_{10} = 8.53 N_{CO,16} \overline{\frac{f_0}{b_5}\left(1 - \frac{r_{10}}{3}\right)} \tag{22}$$

and

$$\tau_{21} = 5.68 N_{CO,16} \overline{\frac{f_1}{b_5}\left(1 - \frac{3r_{21}}{5}\right)}, \tag{23}$$

where $b_5 \equiv b/(10^5 \text{ cm s}^{-1})$. We numerically calculate the n_{CO}-weighted LOS average terms in Equations (22) and (23) and show them as functions of N_{CO} in the middle panels of Figure 7.

Adopting characteristic values $b_5 = 2$ and $T_{exc} = 10$ K, we expect $\tau_{10} = 1$ at $N_{CO} \sim 2.1 \times 10^{16}$ cm^{-2} and $\tau_{21} = 1$ at $N_{CO} \sim 1.2 \times 10^{16}$ cm^{-2}, respectively. This analytic estimate agrees well with our results (except for the $Z' = 0.1$ case where the T_{exc} is much higher). At higher N_{CO}, the lines become optically thick and thus both W_{10} and W_{21} start to flatten and scale sub-linearly with N_{CO}.

At a given N_{CO}, τ_{10} decreases with Z'. This is caused by the corresponding higher density ($\bar{n}$) that more efficiently excites the upper level $J = 1$, which means (i) higher r_{10} and thus more efficient stimulated emission and (ii) lower f_0 as the ground level $J = 0$ is depopulated. In other words, CO(1–0) becomes increasingly optically thin as Z' decreases. In particular, at $Z' = 0.1$, τ_{10} never exceeds unity at all N_{CO}. On the other hand, τ_{21} shows a similar dependency on Z', but the effect is less significant than for τ_{10}, as f_1 does not vary with N_{CO} as much as f_0. Therefore, at $Z' = 0.1$, τ_{21} does eventually become optically thick, reaching a maximum of three at the highest N_{CO}.

Observationally, the excitation temperature of CO(1–0) can be estimated from the peak of the observed radiation temperature $T_{R,max}$ (e.g., Pineda et al. 2008). This is based on

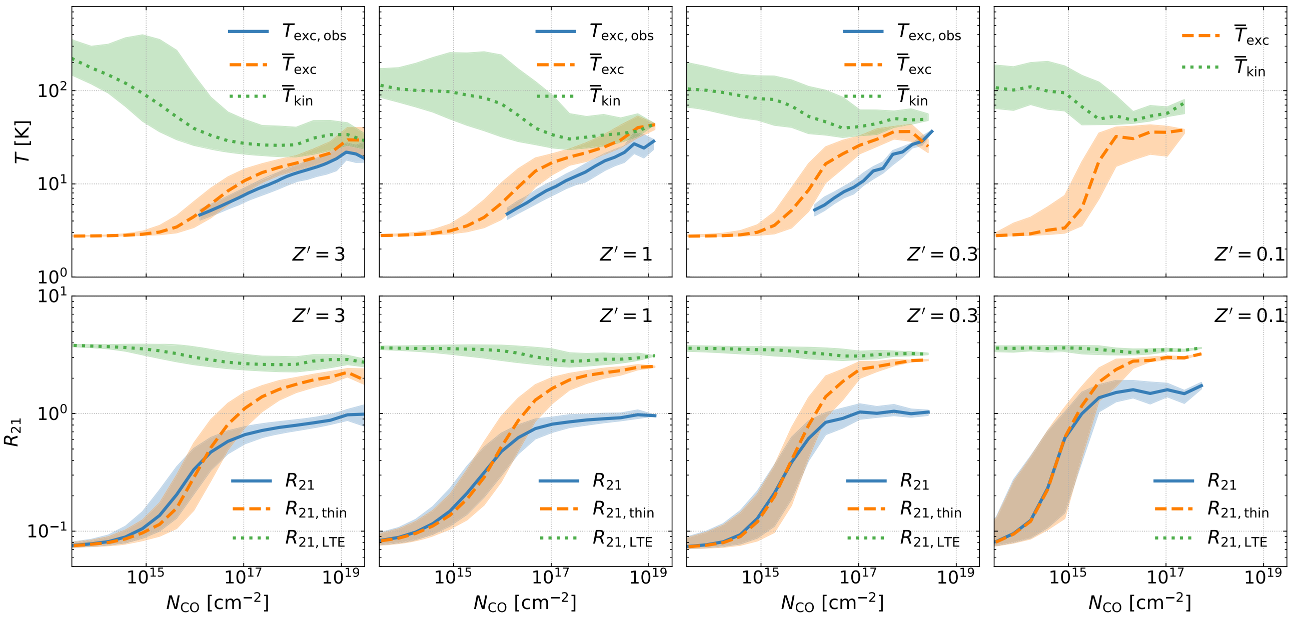

Figure 8. Upper panels: cloud surface excitation temperature as would be observed (blue solid, see Equation (25)), CO density-weighted average excitation temperature (orange dashed, see Equation (26)), and CO density-weighted average kinetic temperature (green dotted, see Equation (27)) as functions of $N_{\rm CO}$ for $Z' = 3$, 1, 0.3, and 0.1 from left to right. Lower panels: observed line ratio $R_{21} \equiv W_{21}/W_{10}$ (blue solid), *optically thin* line ratio (orange dashed, see Equation (28)), and optically thin line ratio assuming LTE (green dotted, see Equation (29)) as functions of $N_{\rm CO}$ for $Z' = 3$, 1, 0.3, and 0.1 from left to right. The lines represent the median values while the shaded areas enclose the 25th and 75th percentiles in all panels. The observed excitation temperature and line ratio are slightly lower than the LOS averages as only the cloud surfaces can be seen for optically thick lines.

the radiative transfer equation in a uniform medium:

$$T_{\rm R} = T_{10}\left(\frac{1}{e^{T_{10}/T_{\rm exc}} - 1} - \frac{1}{e^{T_{10}/T_{\rm bg}} - 1}\right)(1 - e^{-\tau}). \tag{24}$$

If the line is sufficiently optically thick ($\tau \gg 1$), the excitation temperature can be expressed as

$$T_{\rm exc,s} = \frac{T_{10}}{\ln\left(1 + T_{10}\Big/\left(T_{\rm R,max} + \frac{T_{10}}{e^{T_{10}/T_{\rm bg}} - 1}\right)\right)}. \tag{25}$$

In reality, however, molecular clouds are highly inhomogeneous. As long as the line is optically thick, one can only observe emission that originates from the cloud surface up to a thickness of $\tau \approx 1$ where the density is lower and thus $T_{\rm exc}$ is lower. Therefore, Equation (25) only measures the excitation temperature at the cloud surface (and hence the subscript "s"). In the upper panels of Figure 8, the blue solid lines show $T_{\rm exc,s}$ as a function of $N_{\rm CO}$ for $Z' = 3$, 1, 0.3, and 0.1 from left to right. Note that we only show $T_{\rm exc,s}$ in the optically thick regime ($\tau_{10} > 1$) where Equation (25) is applicable. At $Z' = 0.1$, $\tau_{10} < 1$ everywhere and thus $T_{\rm exc,s}$ is not shown. Comparing with the $n_{\rm CO}$-weighted LOS average excitation temperature:

$$\overline{T}_{\rm exc} \equiv \frac{\int n_{\rm CO} T_{\rm exc}\, dz}{\int n_{\rm CO}\, dz}, \tag{26}$$

as shown by the orange dashed lines, we see that $T_{\rm exc,s}$ is indeed slightly lower than $\overline{T}_{\rm exc}$ though the effect is mild (less than a factor of 2). Finally, the green dotted lines are the $n_{\rm CO}$-weighted LOS average kinetic temperature:

$$\overline{T}_{\rm kin} \equiv \frac{\int n_{\rm CO} T_{\rm kin}\, dz}{\int n_{\rm CO}\, dz}. \tag{27}$$

$\overline{T}_{\rm exc}$ gradually increases and approaches $\overline{T}_{\rm kin}$ as $N_{\rm CO}$ increases. Note that $\overline{T}_{\rm exc} < \overline{T}_{\rm kin}$ at almost all $N_{\rm CO}$. Therefore, the fact that $\overline{T}_{\rm exc}$ (and thus $T_{\rm exc,s}$) increases with $N_{\rm CO}$ is mainly driven by the increase of average density instead of a temperature effect as $\overline{T}_{\rm kin}$ is nearly constant. This also explains why W_{10} does not scale as $\ln(N_{\rm CO})$ in the optically thick regime ($N_{\rm CO} \gtrsim 10^{16}\,{\rm cm}^{-2}$), as the theory of curve of growth would predict. Instead, W_{10} increases more rapidly with $N_{\rm CO}$ (see Figure 7), as $T_{\rm exc,s}$ provides an extra contribution to the growth of W_{10}.

Similarly, the lower panels of Figure 8 show the line ratio (R_{21}) in blue solid lines as a function of $N_{\rm CO}$ for $Z' = 3$, 1, 0.3, and 0.1 from left to right. The optically thin line ratio

$$R_{21,\rm thin} \equiv \frac{W_{21,\rm thin}}{W_{10,\rm thin}} = 2.4\frac{\overline{f_2}}{\overline{f_1}} \tag{28}$$

(from Equations (18) and (19)) is shown by orange dashed lines while the *LTE optically thin* line ratio

$$R_{21,\rm LTE}(\overline{T}_{\rm kin}) \equiv 2.4\frac{\overline{f_2}(\overline{T}_{\rm kin})}{\overline{f_1}(\overline{T}_{\rm kin})} \tag{29}$$

is shown by green dotted lines.

In the optically thin regime, $R_{21} = R_{21,\rm thin}$ by definition. At the lowest $N_{\rm CO}$, the excitation is set by the CMB temperature and therefore $R_{21} = R_{21,\rm thin} = 2.4 f_2(2.73)/f_1(2.73) = 0.069$. As $N_{\rm CO}$ increases, the average density also increases which gradually drives $R_{21,\rm thin}$ toward $R_{21,\rm LTE}$, similar to the behavior of r_{21} shown in Figure 6. The maximum of $R_{21,\rm thin}$ is $\sim$2.5 and

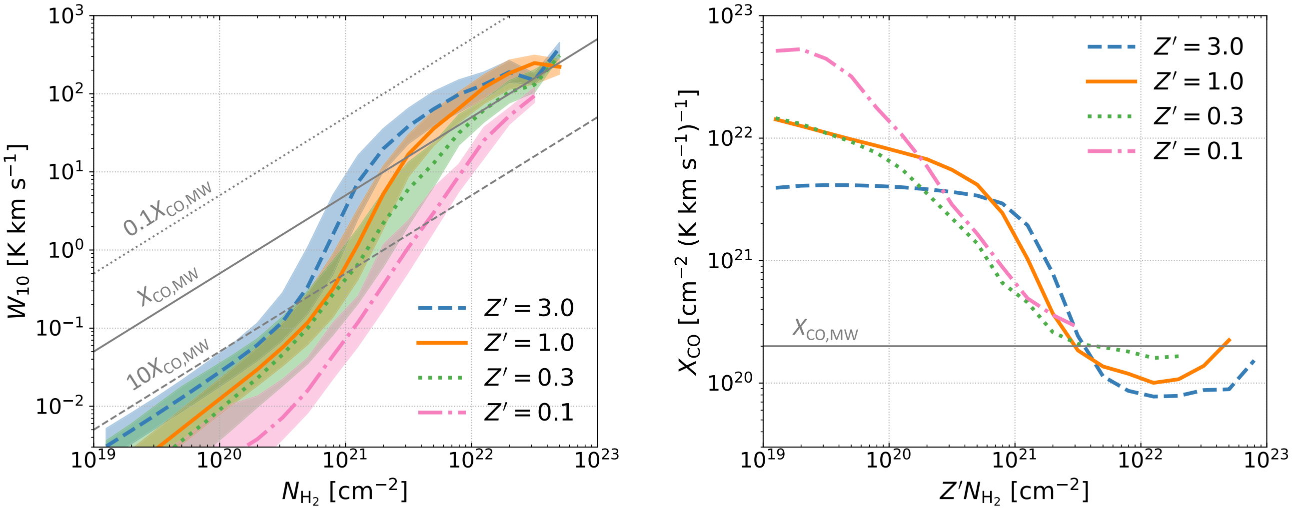

Figure 9. Left panel: CO(1–0) line intensity as a function of H_2 column density (N_{H_2}). The lines represent the median values while the shaded areas enclose the 25th and 75th percentiles. The dotted, solid, and dashed lines in gray indicate $X_{CO}/X_{CO,MW} = 0.1$, 1, and 10, respectively. The variation of X_{CO} is mainly driven by the variation of CO abundance. Right: X_{CO} as a function of $Z'N_{H_2}$. The scatter is not shown for clarity. X_{CO} drops to the Milky Way value ($X_{CO,MW}$, horizontal gray line) at $Z'N_{H_2} \sim 3 \times 10^{21}$ cm^{-3} (visual extinction $A_V \sim 3$) where dust shielding becomes effective.

is insensitive to Z' (as is the case for r_{21}). Note that the maximum theoretical line ratio is $R_{21,\mathrm{LTE}}(\infty) = 4$. In addition, at lower Z', R_{21} rises up at a lower N_{CO} because of the density effect as shown in Figure 7. At high N_{CO}, R_{21} falls slightly below $R_{21,\mathrm{thin}}$ by about a factor of 2 due to the optical depth effect: as both lines become optically thick, the observed R_{21} originates from the cloud surfaces with thickness of $\tau \approx 1$, where the density is lower and the level population is more subthermal. However, at $Z' = 0.1$, both lines are only marginally optically thick and thus R_{21} becomes closer to its optically thin limit $R_{21,\mathrm{thin}}$, reaching a maximum of ∼1.5, (about 50% larger than the higher Z' cases).

5. Observational Implications

5.1. Spatially Resolved X_{CO} and R_{21}

Armed with the detailed background in Section 4, we are now in a good position to study the small-scale distributions of X_{CO} and R_{21}. The left panel of Figure 9 shows W_{10} as a function of N_{H_2} at different Z'. The dotted, solid, and dashed lines in gray indicate $X_{CO}/X_{CO,MW} = 0.1$, 1, and 10, respectively. Recall from Figure 7 that $W_{10} < 10$ K km s^{-1} (or $N_{CO} < 10^{16}$ cm^{-3}) is the optically thin regime where $W_{10} \propto N_{CO}$. It is also in this regime that X_{CO} varies the most, which corresponds to the formation of CO (see Figure 5). At $W_{10} > 10$ K km s^{-1}, the line becomes optically thick and W_{10} flattens, except for the $Z' = 0.1$ case where the line remains optically thin. In this optically thick regime, X_{CO} only varies mildly. Therefore, the variation of X_{CO} mostly occurs in the optically thin regime and is driven by the variation of CO abundance. Note that even at $Z' = 0.1$, X_{CO} eventually reaches $X_{CO,MW}$ at the highest N_{H_2}. In fact, if we plot X_{CO} as a function of $Z'N_{H_2}$, as in the right panel of Figure 9, we see that for all Z', X_{CO} drops to $X_{CO,MW}$ (the horizontal gray line) at $Z'N_{H_2} \sim 3 \times 10^{21}$ cm^{-3}, which corresponds to a visual extinction $A_V \sim 3$ and is where dust shielding becomes effective. This is qualitatively consistent with the cloud-scale simulations in Shetty et al. (2011a).

Figure 10 shows the probability density functions (PDFs) of X_{CO} (left panel) and R_{21} (right panel) at different Z'. The area-weighted PDFs are shown in blue while the W_{10}-weighted PDFs are shown in orange. Most cloud area is filled by diffuse gas with high X_{CO} and low R_{21}, while most CO(1–0) emission originates from dense gas with low X_{CO} and high R_{21}.

As X_{CO} is a distribution rather than a constant, if we want choose a statistical quantity to represent the distribution, a natural choice would be the W_{10}-weighted average (as shown by the red horizontal bars):

$$\langle X_{CO} \rangle_W \equiv \frac{\int X_{CO} W_{10}\, da}{\int W_{10}\, da} = \frac{\sum_i X_{CO,i} W_{10,i}}{\sum_i W_{10,i}}, \tag{30}$$

where the summation is over the 512^2 beams. On the other hand, the conversion factor in a coarse beam of size l_b can be expressed as

$$X_{CO}(l_b) = \frac{N_{H_2}(l_b)}{W_{10}(l_b)} = \frac{\sum_i N_{H_2,i}}{\sum_i W_{10,i}} = \frac{\sum_i X_{CO,i} W_{10,i}}{\sum_i W_{10,i}}, \tag{31}$$

where the summation is over all sub-beams within a coarse beam. Therefore, $\langle X_{CO} \rangle_W$ is also the global conversion factor for the entire (1 kpc)^2 area shown in Figure 1. Similarly, the global W_{10}-weighted average of R_{21} (red horizontal bars) is

$$\langle R_{21} \rangle_W \equiv \frac{\int R_{21} W_{10}\, da}{\int W_{10}\, da} = \frac{\sum_i R_{21,i} W_{10,i}}{\sum_i W_{10,i}}. \tag{32}$$

Since the line ratio in a coarse beam of size (l_b) can be written as

$$R_{21}(l_b) = \frac{W_{21}(l_b)}{W_{10}(l_b)} = \frac{\sum_i W_{21,i}}{\sum_i W_{10,i}} = \frac{\sum_i R_{21,i} W_{10,i}}{\sum_i W_{10,i}}, \tag{33}$$

where the summation is over all sub-beams within a coarse beam, $\langle R_{21} \rangle_W$ is also the global line ratio for the entire (1 kpc)^2 area.

5.2. Scale Dependence

The left panels in Figure 11 show the relationships between N_{H_2} and N_{CO} at different beam sizes for $Z' = 1$. The dashed

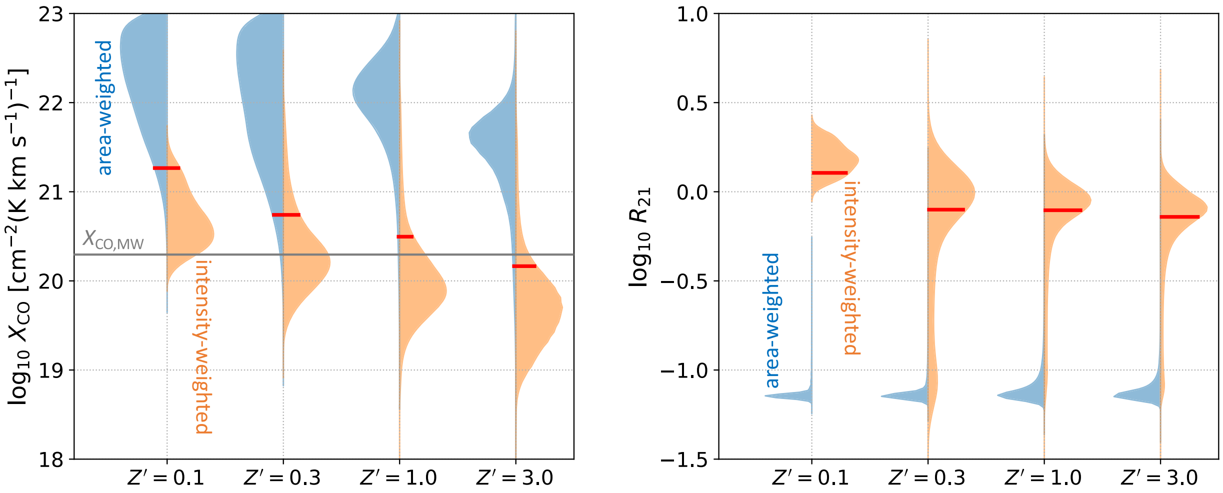

Figure 10. PDFs of $X_{\rm CO}$ (left panel) and R_{21} (right panel) at different Z'. The area-weighted PDFs are shown in blue while the W_{10}-weighted PDFs are shown in orange. The W_{10}-weighted average of $X_{\rm CO}$ (Equation (30)) and R_{21} (Equation (32)) are indicated by the red bars. The Milky Way value of $X_{\rm CO}$ is shown by the horizontal gray line. Most cloud area is filled by diffuse gas with high $X_{\rm CO}$ and low R_{21}, while most CO(1–0) emission originates from dense gas with low $X_{\rm CO}$ and high R_{21}.

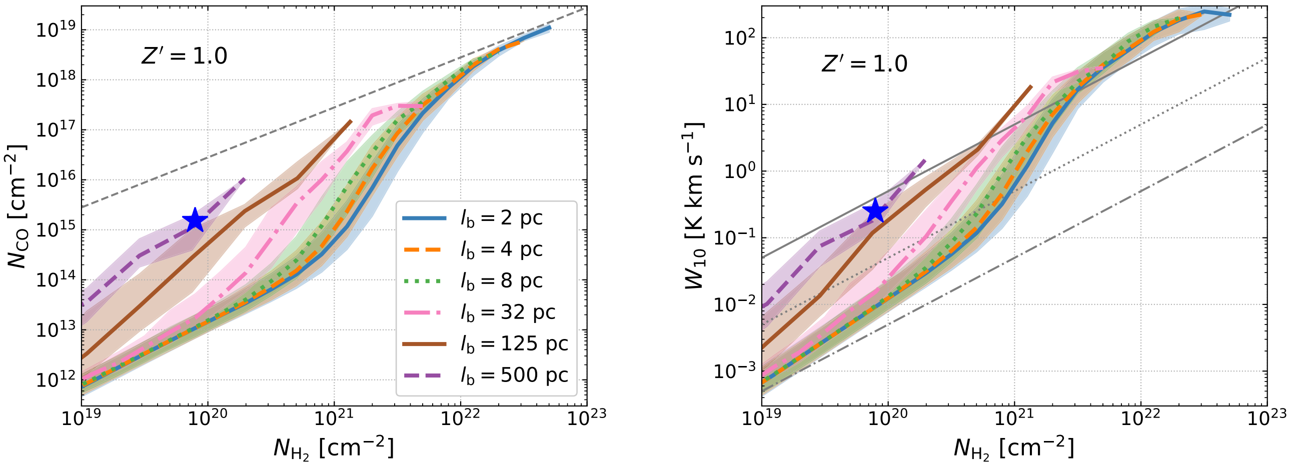

Figure 11. Left panel: relationships between $N_{\rm H_2}$ and $N_{\rm CO}$ at different beam sizes ($l_{\rm b}$) for $Z' = 3$, 1, 0.3, and 0.1 (from top to bottom). The lines represent the median values while the shaded areas enclose the 25th and 75th percentiles. The dashed gray lines indicate $N_{\rm CO} = 2N_{\rm H_2}x_{\rm C,0}$ where hydrogen and carbon are fully in the forms of H$_2$ and CO, respectively. Right panel: same as the left panel, but with W_{10} in the y-axis. The solid, dotted, and dashed–dotted lines in gray indicate $X_{\rm CO}/X_{\rm CO,MW} = 1$, 10, and 100, respectively, where $X_{\rm CO,MW} = 2 \times 10^{20}$ cm^{-2} (K km s^{-1})$^{-1}$ is the canonical CO-to-H$_2$ conversion factor. The blue star symbols indicate the time-averaged values with $l_{\rm b} = 1$ kpc.

gray lines indicate $N_{\rm CO} = 2N_{\rm H_2}x_{\rm C,0}$, which is the upper limit of $N_{\rm CO}$ when carbon is completely in form of CO.

On large scales, a coarse beam contains a distribution of $N_{\rm H_2}$ and $N_{\rm CO}$, and the CO-to-H$_2$ ratio can be expressed as

$$\gamma(l_{\rm b}) = \frac{N_{\rm CO}(l_{\rm b})}{N_{\rm H_2}(l_{\rm b})} = \frac{\sum_i N_{{\rm CO},i}}{\sum_i N_{{\rm H_2},i}} = \frac{\sum_i \gamma_i N_{{\rm H_2},i}}{\sum_i N_{{\rm H_2},i}}, \tag{34}$$

where the summation is over all sub-beams within a coarse beam. Namely, the coarse-beam γ is the $N_{\rm H_2}$-weighted average of the small-scale γ over the sub-beam distribution and the dense, CO-rich gas (where γ is high) has a dominant contribution to the coarse-beam γ. Since γ increases monotonically with $N_{\rm H_2}$, the coarse-beam γ increases with $l_{\rm b}$ at a given $N_{\rm H_2}$. In addition, the variation of γ decreases as $l_{\rm b}$ increases because of beam averaging/smoothing.

Qualitatively, the $N_{\rm H_2}$–W_{10} relation, which we show in the right panels of Figure 11, is very similar to the $N_{\rm H_2}$–$N_{\rm CO}$ relation. The solid, dotted, and dashed–dotted lines in gray indicate $X_{\rm CO}/X_{\rm CO,MW} = 1$, 10, and 100, respectively. Recall that the conversion factor in a coarse beam is the W_{10}-weighted average of the small-scale $X_{\rm CO}$ over the sub-beam distribution. If $X_{\rm CO}$ is constant within a coarse beam (even if $N_{\rm H_2}$ and W_{10} are not constant), the coarse-beam conversion factor is unchanged. However, if there is a sub-beam distribution of $X_{\rm CO}$, Equation (31) implies that the dense, CO-bright gas (where $X_{\rm CO}$ is low) has a dominant contribution to the coarse-beam $X_{\rm CO}$. Since W_{10} is a superlinear function of $N_{\rm H_2}$ (i.e., $X_{\rm CO}$ decreases as $N_{\rm H_2}$ increases), the coarse-beam conversion factor decreases with $l_{\rm b}$ at a given $N_{\rm H_2}$. In addition, the variation of $X_{\rm CO}$ decreases as $l_{\rm b}$ increases because of the smoothing/averaging.

As $l_{\rm b}$ decreases, the $N_{\rm H_2}$–W_{10} relationship gradually converges. Convergence occurs when $l_{\rm b}$ is small enough such that $X_{\rm CO}$ is constant within each beam. To achieve this, the transition regions where $X_{\rm CO}$ varies most have to be spatially resolved, which is increasingly challenging as Z' decreases since the CO-bright clouds becomes smaller.

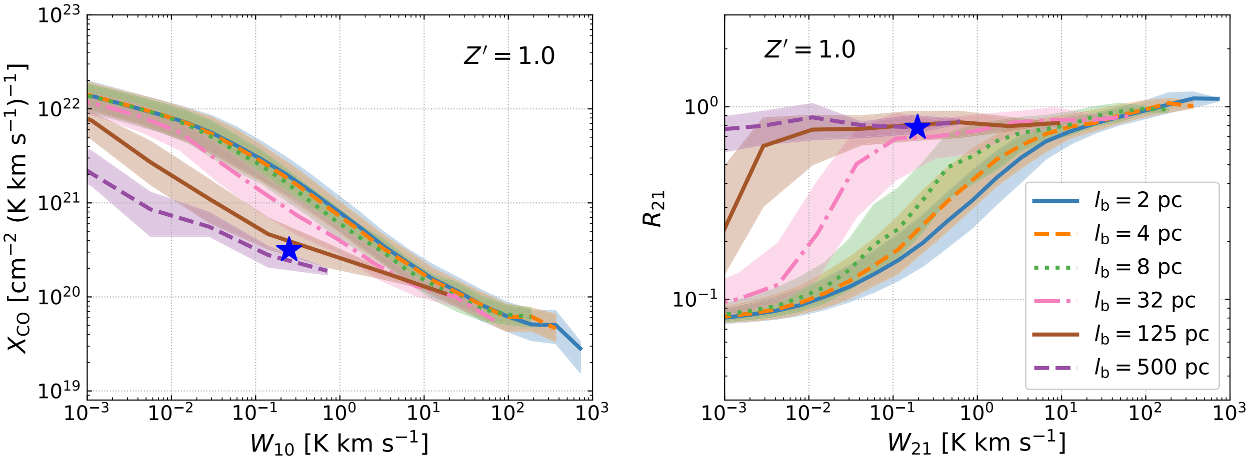

Figure 12. Left panel: X_{CO} as a function of W_{10} with different beam sizes (l_b) for $Z' = 3$, 1, 0.3, and 0.1 (from top to bottom). The lines represent the median values while the shaded areas enclose the 25th and 75th percentiles. Right panel: same as the left panels, but showing the line ratio ($R_{21} \equiv W_{21}/W_{10}$) as a function of W_{21}. The blue star symbols indicate the time-averaged values with $l_b = 1$ kpc.

To make connections with observables, we show X_{CO} as a function of W_{10} in the left panels of Figure 12. The blue star symbol indicates the time-averaged global ($l_b = 1$ kpc) value. On small scales, X_{CO} varies by orders of magnitude. The observed variation depends on the detection threshold. If the threshold intensity $W_{10,th}$ is high (i.e., low sensitivity), the variation of X_{CO} is reduced as only the brightest regions with low X_{CO} can be detected while the diffuse gas becomes "*CO dark*."[9] On the other hand, if we adopt a much lower $W_{10,th}$ (i.e., better sensitivity), X_{CO} can vary by more than an order of magnitude as both low- and high-X_{CO} regions are detected. In this case, adopting a constant X_{CO} (which is typically done in observations) implies that N_{H_2} would be substantially underestimated in diffuse gas and overestimated in dense gas. In other words, the gradient of N_{H_2} would be overestimated.

As l_b decreases, X_{CO} becomes increasingly uniform due to beam averaging and eventually approaches the global value. For example, at $l_b = 125$ pc, X_{CO} only varies by a factor of 2 above $W_{10} = 1$ K km s^{-1}.

The scale dependence of R_{21} can be understood in a similar way, as shown in the right panels of Figure 12. R_{21} in a coarse beam is the W_{10}-weighted average of the small-scale R_{21} over the sub-beam distribution and the dense, thermalized gas (where R_{21} is high) has a dominant contribution to the coarse-beam R_{21}. Since R_{21} increases monotonically with W_{10}, the coarse-beam R_{21} increases with l_b. The variation of R_{21} decreases as l_b increases because of the smoothing/averaging and eventually R_{21} approaches the global average at $l_b = 1$ kpc (blue star symbol).

Figures 11 and 12 focus exclusively on solar metallicity. In Figure 13, we show X_{CO} as a function of W_{10} for different Z' (colored lines) and different l_b (panels). The time-averaged global ($l_b = 1$ kpc) values are shown in stars. On small scales ($l_b = 2$ pc), X_{CO} is a decreasing function of W_{10} with a secondary dependence on Z' most prominent at $W_{10} > 1$ K km s^{-1}. As l_b increases, the W_{10}–X_{CO} relation is shifted downward and rightward. Moreover, the secondary dependence on Z' is gradually reduced for a given W_{10}. At $l_b = 1$ kpc, a single power-law relation holds for all Z', with different Z' populating different ranges of W_{10}. We provide the best-fit formula shown as the red dashed line:

$$X_{CO} = 8.95 \times 10^{19}\left(\frac{W_{10}}{\mathrm{K\ km\ s^{-1}}}\right)^{-0.43} \mathrm{cm^{-2}\ (K\ km\ s^{-1})^{-1}}, \tag{35}$$

with a correlation coefficient of 0.90.

Figure 13 summarizes the key result of this paper and can be used to more accurately infer the H_2 mass from CO(1–0) observations. It highlights the fact that X_{CO} depends not only on Z', but also on W_{10} and l_b. Different observations probe different regimes of the parameter space, leading to discrepancies when projecting on the Z'–X_{CO} plane. For example, observations using the dust-based method or the inverse KS method typically have kiloparsec-scale beam sizes within which the diffuse and dense gas are averaged over, while high-resolution CO observations (the virial method) are naturally biased toward the dense gas as the diffuse gas might be below the detection threshold.

5.3. CO-dark H_2 Fraction

The left panel of Figure 14 shows the cumulative distributions of W_{10} weighted by N_{H_2} (solid) and W_{10} (dashed), respectively. Most CO(1–0) emission is coming from $1 < W_{10} < 100$ K km s^{-1}, while the H_2 mass is distributed in a lower and more widespread range $10^{-2} < W_{10} < 10$ K km s^{-1}. This difference makes CO(1–0) an imperfect tracer of H_2. The N_{H_2}-weighted cumulative distribution can also be interpreted as the CO-dark H_2 *mass* fraction

$$F^m_{\rm dark} \equiv \frac{M_{H_2}(W_{10} < W_{10,th})}{M_{H_2}} \tag{36}$$

as a function of detection threshold ($W_{10,th}$). Adopting $W_{10,th} = 1$ K km s^{-1}, the CO-dark H_2 mass fraction is about

---

[9] Note that we adopt an observational definition of CO dark. Namely, we distinguish between CO-dark gas and high-X_{CO} gas. The former solely reflects the detectability controlled by the detection threshold $W_{10,th}$ and is, in principle, independent of X_{CO}. Gas with low X_{CO} can be CO dark if $W_{10,th}$ is high. Conversely, gas with high X_{CO} can also be CO bright if $W_{10,th}$ is low enough to detect it.

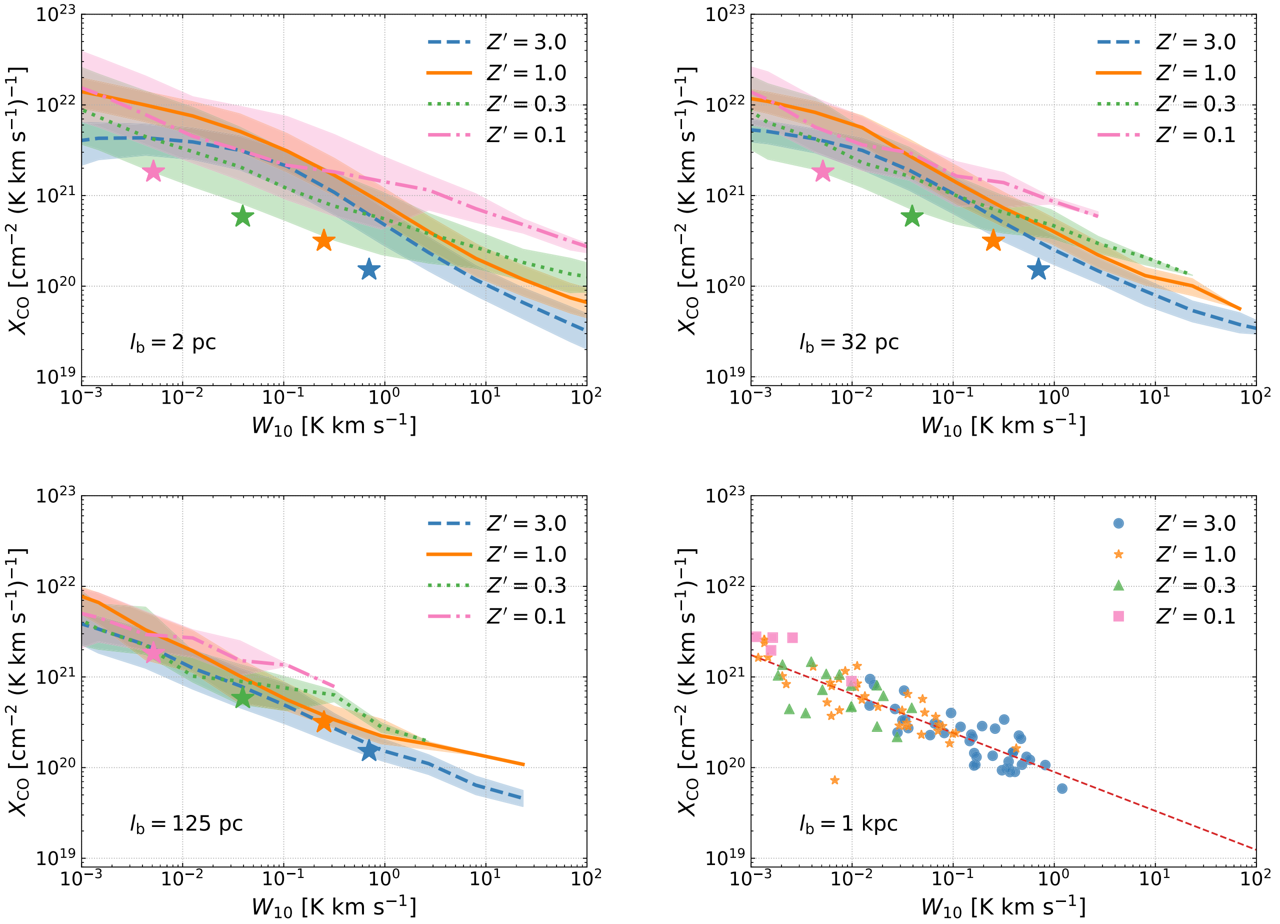

Figure 13. $X_{\rm CO}$ as a function of W_{10} for different Z' (colored lines) and different $l_{\rm b}$ (panels). The lines represent the median values while the shaded areas enclose the 25th and 75th percentiles. The time-averaged global values are shown by the star symbols. The bottom right panel is shown with a scatter plot due to limited data points at $l_{\rm b} = 1$ kpc. The W_{10}–$X_{\rm CO}$ relation at $l_{\rm b} = 1$ kpc can be well described by a single power law (red dashed line, Equation (35)) for all metallicities. This figure can be used to more accurately infer H_2 mass observationally.

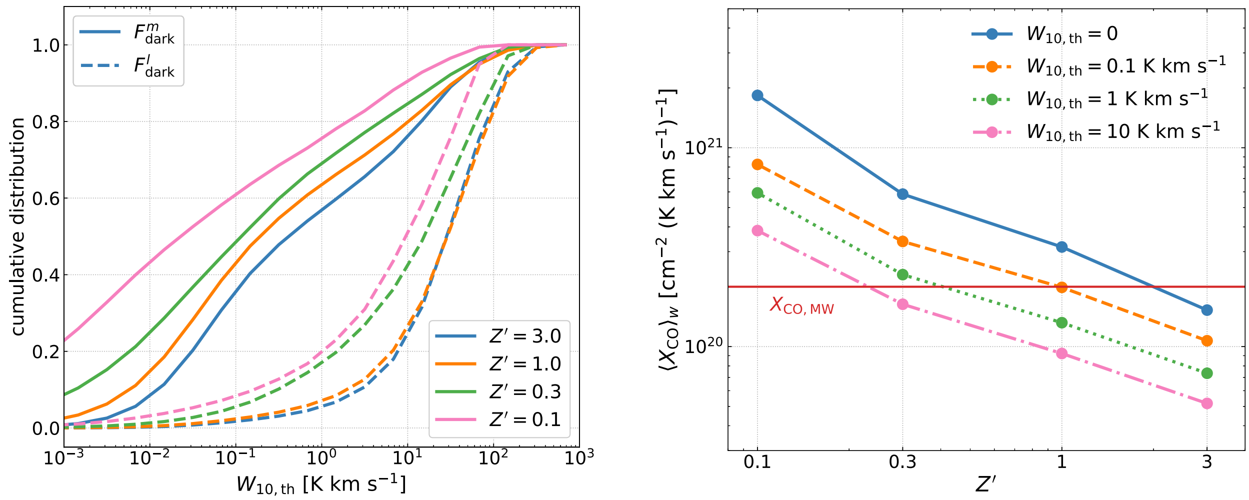

Figure 14. Left panel: CO-dark H_2 mass fraction (solid) and CO-dark light fraction (dashed) as a function of detection threshold $W_{\rm 10,th}$. Right panel: intensity-weighted average $X_{\rm CO}$ as a function of Z' with different detection thresholds. The horizontal line shows the Milky Way value $X_{\rm CO,MW}$. A higher detection threshold leads to a lower $X_{\rm CO,MW}$ as only the brightest gas with low $X_{\rm CO}$ can be detected.

55%–75% from $Z' = 3$–0.1, consistent with HSvD21 where we adopted an $N_{\rm CO}$-equivalent threshold. More than half of the H_2 mass is hidden in the undetected diffuse gas. Similarly, the W_{10}-weighted cumulative distribution can be interpreted as the CO-dark *light* fraction

$$F^l_{\rm dark} \equiv \frac{L_{10}(W_{10} < W_{\rm 10,th})}{L_{10}} \tag{37}$$

Table 1
Global Intensity-weighted Average Quantities

Z' (1)	$\langle X_{\rm CO}\rangle_W$ (2)	$\langle R_{21}\rangle_W$ (3)	$\langle \tau_{10}\rangle_W$ (4)	$\langle \tau_{21}\rangle_W$ (5)	$\langle \overline{T}_{\rm exc,s}\rangle_W$ (6)
3	1.52×10^{20}	0.71	39.0	99.3	11.4
1	3.17×10^{20}	0.78	15.5	42.8	12.3
0.3	5.84×10^{20}	0.79	3.38	10.8	10.6
0.1	1.83×10^{21}	1.29	0.31	1.38	⋯

Note. (1) Normalized metallicity. (2) CO-to-H$_2$ conversion factor in units of cm^{-2} (K km s^{-1})$^{-1}$. (3) Line ratio of CO(2–1) to CO(1–0). (4) Optical depth of CO(1–0). (5) Optical depth of CO(2–1) (weighted by W_{21} instead of W_{10}). (6) Cloud surface excitation temperature of CO(1–0) in units of K assuming optically thick conditions (see Equation (25)). It is absent in the $Z' = 0.1$ case as CO(1–0) is always optically thin even in the densest gas.

as a function of detection threshold ($W_{10,\rm th}$). For $W_{10,\rm th} = 1$ K km s^{-1}, the CO-dark light fraction is about 5%–20% from $Z' = 3$ to 0.1, i.e., most of the CO(1–0) emission can be detected.

Correspondingly, the intensity-weighted average conversion factor over the detectable beams (i.e., $W_{10} \geqslant W_{10,\rm th}$) as a function of Z' is shown in the right panel of Figure 14. The Milky Way value $X_{\rm CO,MW}$ is shown by the horizontal red line. As the CO-bright H$_2$ mass fraction is $1 - F^m_{\rm dark}$ and the CO-bright light fraction is $1 - F^l_{\rm dark}$, the intensity-weight conversion factor above a detection threshold $W_{10,\rm th}$ follows

$$\langle X_{\rm CO}(W_{10} \geqslant W_{10,\rm th})\rangle_W = \frac{1 - F^m_{\rm dark}}{1 - F^l_{\rm dark}} \langle X_{\rm CO}\rangle_W \approx (1 - F^m_{\rm dark}) \langle X_{\rm CO}\rangle_W, \quad (38)$$

where the approximation holds when most of the CO(1–0) emission can be detected (i.e., $1 - F^l_{\rm dark} \approx 1$). For example, if we adopt $W_{10,\rm th} = 1$ K km s^{-1}, then $F^m_{\rm dark} \approx 60\%$, $F^l_{\rm dark} \approx 5\%$, and thus $\langle X_{\rm CO}(W_{10} \geqslant 1\ {\rm K\ km\ s^{-1}})\rangle_W \approx 0.42 \langle X_{\rm CO}\rangle_W$. In general, a higher detection threshold leads to a lower value as only the brightest gas with low $X_{\rm CO}$ can be detected.

Table 1 summarizes several global intensity-weighted average quantities.

6. Summary

We have studied the CO-to-H$_2$ conversion factor and the line ratio of CO(2–1) to CO(1–0) in high-resolution (~0.2 pc) hydrodynamical simulations of a multiphase ISM across a wide range of metallicity ($0.1 \leqslant Z' \leqslant 3$) in HSvD21. We use the radiative transfer code RADMC-3D to post-process CO emission over a 400 Myr time period such that a large number of clouds at different evolutionary stages are properly sampled. We interpolate the particle data onto an adaptive mesh (the code is publicly available[10]) with a minimum cell size of ~0.2 pc to ensure that all small-scale CO emission is properly captured in our radiative transfer calculations, which is particularly important at low metallicities. Our main findings can be summarized as follows:

1. The kiloparsec-scale $X_{\rm CO}$ at low Z' can be overestimated either by assuming steady-state chemistry (e.g., when converting fine structure metal lines and CO lines to an H$_2$ mass via PDR models) or by assuming the star-forming gas is fully molecular (e.g., when using the inverse KS method to convert an SFR to an H$_2$ mass) (see Figure 1). Our fiducial, time-dependent model can be described by Equation (8) on a 1 kpc scale.
2. Instead of a single-variable function of Z', $X_{\rm CO}$ is a multivariate function of three observables: Z', W_{10}, and $l_{\rm b}$ (Figure 13). Observations with different beam sizes and detection thresholds are sensitive to different parts of the parameter space. Comparing $X_{\rm CO}$ between different observations on the Z'–$X_{\rm CO}$ plane can therefore be misleading, and a fair comparison should take all three variables into account.
3. On large scales, the metallicity dependence on the W_{10}–$X_{\rm CO}$ plane is gradually reduced as a result of the sub-beam gas distribution. At $l_{\rm b} = 1$ kpc, a single power-law relation (Equation (35)) holds for all Z', with different Z' populating different ranges of W_{10} (Figure 13).
4. On parsec scales, $X_{\rm CO}$ varies by orders of magnitude from place to place. The variation of $X_{\rm CO}$ occurs primarily in the optically thin regime, driven by the variation of CO abundance in the transition from atomic carbon to CO. The parsec-scale $X_{\rm CO}$ can be well characterized by a single parameter $Z' N_{\rm H_2}$, and it drops to the Milky Way value once dust shielding becomes effective (Figure 9).
5. The line intensities are proxies of column or volume densities and thus can be used to infer $X_{\rm CO}$ and R_{21}. On parsec scales, $X_{\rm CO}$ negatively correlates with W_{10} while R_{21} positively correlates with W_{21} (Figure 12). The large-scale $X_{\rm CO}$ and R_{21} are results of beam averaging, and they are naturally biased toward values in dense gas with low $X_{\rm CO}$ and high R_{21} (Equations (31) and (33)).
6. Most cloud area is filled by diffuse gas with high $X_{\rm CO}$ and low R_{21}, while most CO emission originates from dense gas with low $X_{\rm CO}$ and high R_{21} (Figure 10). Adopting a constant $X_{\rm CO}$ strongly over- (under-)estimates H$_2$ in dense (diffuse) gas.
7. Both CO(1–0) and CO(2–1) are thermalized at higher densities as Z' decreases (Figure 6) because (i) H$_2$ exists at densities higher than the critical densities of the lines, and (ii) the CO abundances and hence the optical depth are lower, which leads to less radiation trapping.
8. The LOS average gas density increases with $N_{\rm CO}$. In addition, as CO only exists at the densest core at low Z', the corresponding LOS average gas density is higher at a given $N_{\rm CO}$. This effect counters the higher thermalization densities such that the CO levels are more efficiently excited at low Z' (Figure 7).
9. The CO lines become increasingly optically thin at lower Z'. This is not only because of the lower CO column densities but also because the levels are more efficiently excited, which leads to a smaller optical depth at a given $N_{\rm CO}$ (Figure 7). In the optically thick regime, the line intensities increase faster than $\ln N_{\rm CO}$ (as the curve of growth theory would predict) because the excitation temperature also increases with $N_{\rm CO}$ and gradually approaches the kinetic temperature due to the increase in the LOS average density.
10. The excitation temperature derived from the peak radiation temperature (Equation (25)) is subthermal (Figure 8 and Table 1). At $Z' = 0.1$, Equation (25) is

---

[10] https://github.com/huchiayu/ParticleGridMapper.jl

no longer applicable as the optically thick assumption breaks down. In addition, R_{21} increases as the lines become increasingly optically thin.

11. The intensity-weighted average $X_{\rm CO}$ is controlled by the CO-dark H_2 mass fraction and the CO-dark light fraction (Figure 14 and Equation (38)), and it decreases with the detection threshold $W_{10,\rm th}$ as only the brightest gas with low $X_{\rm CO}$ can be detected.

In summary, $X_{\rm CO}$ is a multivariate function of metallicity, line intensity, and beam size. Although we did not find a simple parameterization for this function, our Figure 13 can be used by observers to more accurately infer the H_2 mass in galaxies with similar conditions of the solar neighborhood. It is still unclear to what extent this function is applicable in different environments (e.g., high-redshift galaxies, dwarf galaxies, etc.) where the large-scale physical properties (e.g., gas surface density, turbulence, etc.) are very different. This will be investigated in follow-up studies.

We thank the anonymous referee for the constructive comments that improved our manuscript. C.Y.H. acknowledges support from the DFG via German-Israel Project Cooperation grant STE1869/2-1 GE625/17-1. A.S. thanks the Center for Computational Astrophysics (CCA) of the Flatiron Institute, and the Mathematics and Physical Science (MPS) division of the Simons Foundation for support. All simulations were run on the Raven, Cobra, and Draco supercomputers at the Max Planck Computing and Data Facility (MPCDF).

Appendix A
Scale Dependence of $\langle X_{\rm CO}\rangle_W$

In the case of $W_{10,\rm th} = 0$ (i.e., infinite sensitivity), the global intensity-weighted average $\langle X_{\rm CO}\rangle_W$ is by construction independent of $l_{\rm b}$ as beam averaging is equivalent to the W_{10}-weighted average over the sub-beam distribution (see Equations (30) and (31)). However, if we consider a nonzero $W_{10,\rm th}$, $\langle X_{\rm CO}\rangle_W$ is only averaged over the CO-bright beams where $W_{10} > W_{10,\rm th}$ and thus does depend on $l_{\rm b}$, as shown in Figure 15. At a given $l_{\rm b}$, $\langle X_{\rm CO}\rangle_W$ decreases inversely with $W_{10,\rm th}$ as the faint, high $X_{\rm CO}$ gas becomes CO dark and only the bright, low $X_{\rm CO}$ gas can be detected. With $W_{10,\rm th} = 0$, $\langle X_{\rm CO}\rangle_W$ is indeed (by construction) independent of $l_{\rm b}$. With a finite $W_{10,\rm th}$, there is a very mild $l_{\rm b}$ dependence that arises from two competing effects. On one hand, a coarse beam averages over CO-bright and CO-dark gas. As CO emission predominately originates from the CO-bright gas, the coarse-beam intensity is likely to exceed the detection threshold. Namely, the entire coarse beam becomes CO bright, which effectively includes the fine-grained CO-dark gas within the beam to the global average, leading to an increase in $\langle X_{\rm CO}\rangle_W$ as CO-dark gas tends to be of high $X_{\rm CO}$. On the other hand, when the beam size is so large that the majority of the area is filled with CO-dark gas, the dilution effect can be strong enough such that the entire coarse beam becomes CO dark, which effectively excludes the fine-grained CO-bright gas within the beam from the global average. Therefore, as $l_{\rm b}$ increases, $\langle X_{\rm CO}\rangle_W$ first increase at small $l_{\rm b}$ and then decreases at large $l_{\rm b}$. The effect is very mild, within 30% from $l_{\rm b} = 2$ pc to $l_{\rm b} = 1$ kpc. In short, $\langle X_{\rm CO}\rangle_W$ mainly depends on the detection threshold (as shown in Figure 14) and is nearly scale independent.

Similarly, Figure 16 demonstrates the scale dependence of the global average line ratio $\langle R_{21}\rangle_W$ (see Equation (32)) with different detection thresholds $W_{21,\rm th}$. $\langle R_{21}\rangle_W$ is nearly scale independent and it increases with $W_{21,\rm th}$ as R_{21} tends to be high in CO-bright gas. However, the variation is very weak, less than 20% in all cases.

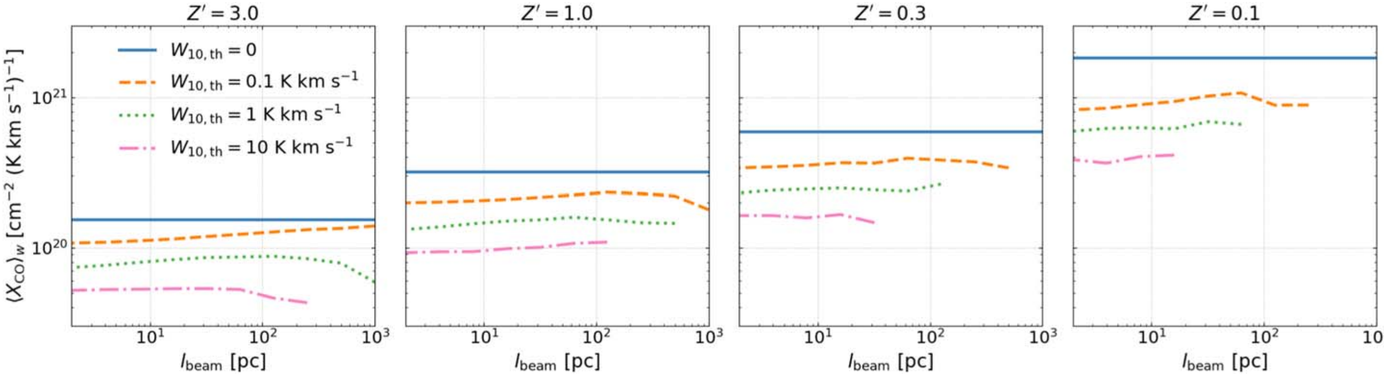

Figure 15. Global intensity-weighted average CO-to-H_2 conversion factor as a function of beam size with different detection thresholds $W_{10,\rm th}$ at $Z' = 3$, 1, 0.3, and 0.1 from left to right.

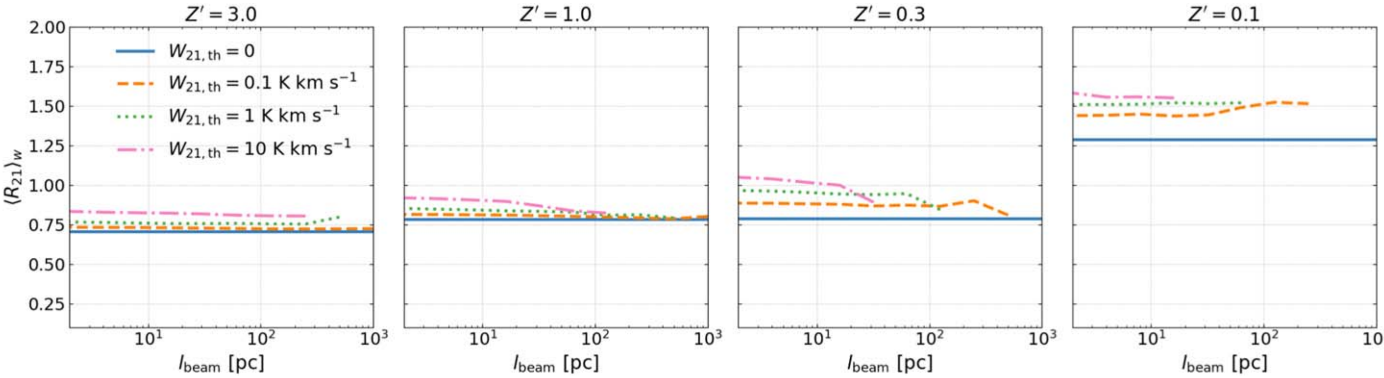

Figure 16. Global intensity-weighted average line ratio as a function of beam size with different detection thresholds $W_{21,\rm th}$ at $Z' = 3$, 1, 0.3, and 0.1 from left to right.

Appendix B
Scale Dependence of the CO-dark Gas

For a given $W_{10,\rm th}$, $\langle X_{\rm CO}\rangle_W$ only accounts for H_2 in the CO-bright beams, while a significant amount of H_2 may be hidden in the CO-dark beams. Figure 17 shows the CO-dark H_2 mass fraction ($F^m_{\rm dark}$, upper row) and CO-dark light fraction ($F^l_{\rm dark}$, lower row) as a function of detection threshold $W_{10,\rm th}$ at different beam sizes $l_{\rm b}$ for $Z' = 3$, 1, 0.3, and 0.1 from left to right. As $l_{\rm b}$ increases, the CDF becomes narrower due to beam smoothing and gradually approaches a step function. Therefore, $F^m_{\rm dark}$ may increase or decrease as $l_{\rm b}$ increases, depending on the detection threshold. For $W_{10,\rm th} = 1$ K km s^{-1}, $F^m_{\rm dark}$ remains almost constant at small $l_{\rm b}$ where the distribution is converged. At $l_{\rm b} \gtrsim 32$ pc, $F^m_{\rm dark}$ increases with $l_{\rm b}$ as the beam averaging makes the fine-grained CO-bright gas undetectable. Similarly, $F^l_{\rm dark}$ remains constant at small $l_{\rm b}$ and increase with $l_{\rm b}$ at $l_{\rm b} \gtrsim 32$ pc. This provides another explanation of why $\langle X_{\rm CO}\rangle_W$ is insensitive to $l_{\rm b}$, as both $F^m_{\rm dark}$ and $F^l_{\rm dark}$ begin to increase at $l_{\rm b} \gtrsim 32$ pc and they cancel out (see Equation (38)).

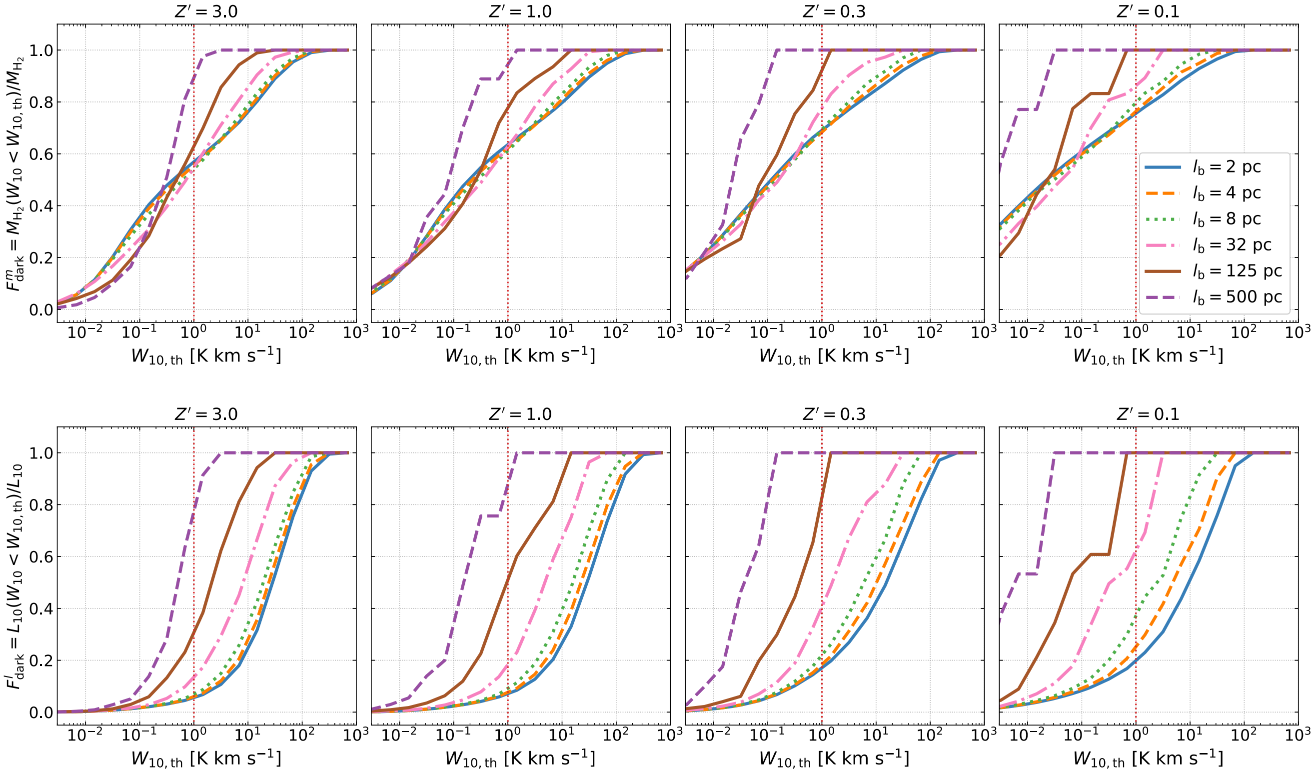

Figure 17. CO-dark H_2 mass fraction (upper row) and CO-dark light fraction (lower row) as a function of detection threshold $W_{10,\rm th}$ at different beam sizes l_b for $Z' = 3$, 1, 0.3, and 0.1 from left to right.

Appendix C
CO(1–0) Spectrum

Figure 18 shows 2500 CO(1–0) spectra randomly drawn from the 512×512 pixels in the $Z' = 1$ run at $t = 420$ Myr. Gas motion leads to a variety of spectrum profiles, including Gaussian-like, skewed, saturated, or even double-peaked. Our adopted spectrum resolution (0.4 km s^{-1}) is sufficient to resolve the typical line width of the spectra, and our spectrum coverage (40 km s^{-1}) is large enough to include all the CO(1–0) emission.

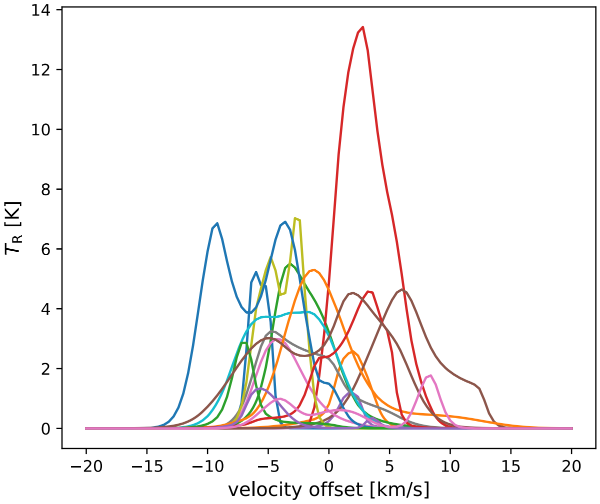

Figure 18. CO(1–0) spectra randomly drawn from the 512 × 512 pixels in the $Z' = 1$ run at $t = 420$ Myr. Gas motion leads to a variety of spectrum profiles, including Gaussian-like, skewed, saturated, or even double-peaked.

Appendix D
Interpolation Scheme

In this appendix, we compare three different interpolation schemes that map Lagrangian (particle) data onto a mesh. For a given particle distribution, where a particle i carries information of mass (m_i), gas density (ρ_i), smoothing length (h_i), and a scalar field (A_i) at location x_i. The standard SPH scheme interpolate the scalar field at location x_c as

$$\bar{A}_{\rm SPH}(x_c) = \sum_j \frac{m_j}{\rho_j} A_j K(|x_j - x_c|, h_j), \quad \text{(D1)}$$

where the summation is over the *scatter* neighboring particles j. This scheme has the drawback that a constant scalar field would be interpolated as nonconstant, as $\sum_j \frac{m_j}{\rho_j} K(|x_j - x_c|, h_j)$, in general, does not sum up to unity. This can be remedied by the normalized SPH scheme:

$$\bar{A}_{\rm nSPH}(x_c) = \frac{\sum_j \frac{m_j}{\rho_j} A_j K(|x_j - x_c|, h_j)}{\sum_j \frac{m_j}{\rho_j} K(|x_j - x_c|, h_j)}, \quad \text{(D2)}$$

which factors out the non-unity term. Alternatively, one can use the MFM scheme:

$$\bar{A}_{\rm MFM}(x_c) = \frac{\sum_j A_j K(|x_j - x_c|, h_j)}{\sum_j K(|x_j - x_c|, h_j)}. \quad \text{(D3)}$$

Similar to the normalized SPH scheme, the MFM scheme interpolates a constant field as constant.

In Figure 19, the left panels of show the mass-weighted PDFs of hydrogen number density (n, upper panel) and temperature (T, lower panel) for the particle data and the three interpolation schemes. The middle and right panels show the mass-weighted *phase diagram* (heatmap of n versus T) for the particle data and the three interpolation schemes.

While all schemes reproduce the actual density distribution from the particle data, both the standard SPH scheme and normalized SPH scheme significantly overproduce the hot gas ($10^4 < T < 10^6$ K) and underproduce the cold gas ($10 < T < 10^3$ K). This is caused by the volume factor m_j/ρ_j, which put a strong weighting on the diffuse gas (low ρ_j). For density interpolation, the ρ_j dependence cancels out. For temperature interpolation, as the diffuse gas typically has a high T, the contribution from the hot gas is enormous, and thus the result is generally biased high.

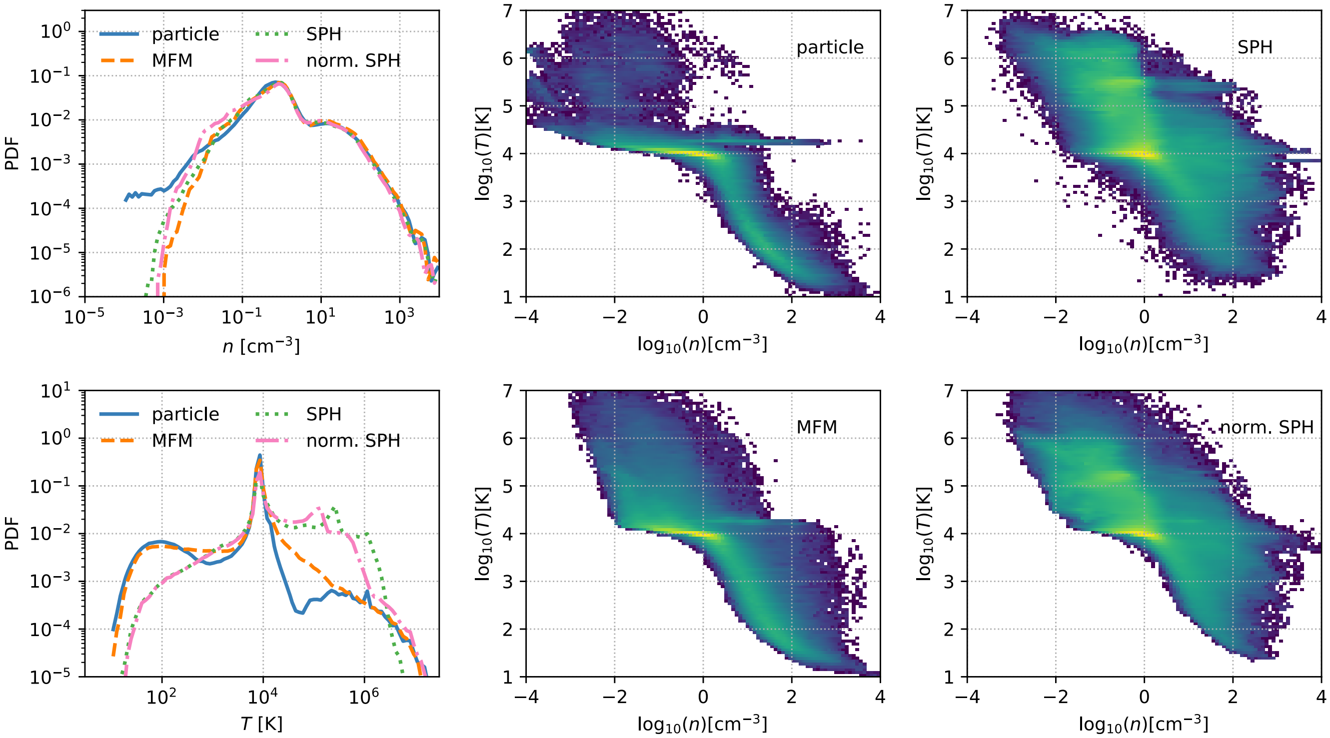

Figure 19. Left panels: mass-weighted PDFs of hydrogen number density (n, upper panel) and temperature (T, lower panel) for the particle data, the standard SPH scheme (Equation (D1)), the normalized SPH scheme (Equation (D2)), and the MFM scheme (Equation (D3)). Middle and right panels: *phase diagram* (heatmap of n vs. T) for the particle data and the three interpolation schemes. The MFM scheme faithfully reproduces the distributions of n and T, while the two SPH schemes significantly over-estimate T.

In contrast, the MFM scheme depends merely on particle configuration (which defines h_j) and is independent of m_j and ρ_j. This means that the diffuse gas does not have the same strong weighting as in the SPH schemes, and thus the temperature distribution is more faithfully reproduced.

ORCID iDs

Chia-Yu Hu (胡家瑜) https://orcid.org/0000-0002-9235-3529
Amiel Sternberg https://orcid.org/0000-0001-5065-9530
Ewine F. van Dishoeck https://orcid.org/0000-0001-7591-1907

References

Accurso, G., Saintonge, A., Catinella, B., et al. 2017, MNRAS, 470, 4750
Amorín, R., Muñoz-Tuñón, C., Aguerri, J. A. L., & Planesas, P. 2016, A&A, 588, A23
Barnes, J., & Hut, P. 1986, Natur, 324, 446
Bialy, S., & Sternberg, A. 2019, ApJ, 881, 160
Bisbas, T. G., Tan, J. C., & Tanaka, K. E. I. 2021, MNRAS, 502, 2701
Bisbas, T. G., van Dishoeck, E. F., Papadopoulos, P. P., et al. 2017, ApJ, 839, 90
Bolatto, A. D., Jackson, J. M., & Ingalls, J. G. 1999, ApJ, 513, 275
Bolatto, A. D., Leroy, A. K., Rosolowsky, E., Walter, F., & Blitz, L. 2008, ApJ, 686, 948
Bolatto, A. D., Wolfire, M., & Leroy, A. K. 2013, ARA&A, 51, 207
Clark, P. C., Glover, S. C. O., & Klessen, R. S. 2012, MNRAS, 420, 745
Cormier, D., Madden, S. C., Lebouteiller, V., et al. 2014, A&A, 564, A121
den Brok, J. S., Chatzigiannakis, D., Bigiel, F., et al. 2021, MNRAS, 504, 3221
Draine, B. T. 1978, ApJS, 36, 595
Draine, B. T. 2011, Physics of the Interstellar and Intergalactic Medium (Princeton, NJ: Princeton Univ. Press)
Duarte-Cabral, A., Acreman, D. M., Dobbs, C. L., et al. 2015, MNRAS, 447, 2144
Dullemond, C. P., Juhasz, A., Pohl, A., et al. 2012, RADMC-3D: A Multi-purpose radiative transfer tool, Astrophysics Source Code Library, ascl:1202.015
Ekström, S., Georgy, C., Eggenberger, P., et al. 2012, A&A, 537, A146
Elmegreen, B. G., Rubio, M., Hunter, D. A., et al. 2013, Natur, 495, 487
Feldmann, R., Gnedin, N. Y., & Kravtsov, A. V. 2012, ApJ, 747, 124
Flower, D. R. 2001, JPhB, 34, 2731
Fuchs, B., Jahreiß, H., & Flynn, C. 2009, AJ, 137, 266
Gaburov, E., & Nitadori, K. 2011, MNRAS, 414, 129
Gatto, A., Walch, S., Naab, T., et al. 2017, MNRAS, 466, 1903
Genzel, R., Tacconi, L. J., Combes, F., et al. 2012, ApJ, 746, 69
Glover, S. C. O., & Clark, P. C. 2012a, MNRAS, 426, 377
Glover, S. C. O., & Clark, P. C. 2012b, MNRAS, 421, 116
Glover, S. C. O., & Mac Low, M.-M. 2007, ApJS, 169, 239
Glover, S. C. O., & Mac Low, M.-M. 2011, MNRAS, 412, 337
Gong, M., Ostriker, E. C., & Kim, C.-G. 2018, ApJ, 858, 16
Gong, M., Ostriker, E. C., Kim, C.-G., & Kim, J.-G. 2020, ApJ, 903, 142
Górski, K. M., & Hivon, E. 2011, HEALPix: Hierarchical equal area isolatitude pixelization of a sphere, Astrophysics Source Code Library, ascl:1107.018
Heays, A. N., Bosman, A. D., & van Dishoeck, E. F. 2017, A&A, 602, A105
Hopkins, P. F. 2015, MNRAS, 450, 53
Hu, C.-Y., Naab, T., Glover, S. C. O., Walch, S., & Clark, P. C. 2017, MNRAS, 471, 2151
Hu, C.-Y., Sternberg, A., & van Dishoeck, E. F. 2021, ApJ, 920, 44
Hunt, L. K., García-Burillo, S., Casasola, V., et al. 2015, A&A, 583, A114
Indriolo, N., & McCall, B. J. 2012, ApJ, 745, 91
Indriolo, N., Neufeld, D. A., Gerin, M., et al. 2015, ApJ, 800, 40
Kroupa, P. 2001, MNRAS, 322, 231
Lada, C. J., & Lada, E. A. 2003, ARA&A, 41, 57
Lee, C., Leroy, A. K., Schnee, S., et al. 2015, MNRAS, 450, 2708
Lejeune, T., Cuisinier, F., & Buser, R. 1997, A&AS, 125, 229
Lejeune, T., Cuisinier, F., & Buser, R. 1998, A&AS, 130, 65
Leroy, A. K., Bolatto, A., Gordon, K., et al. 2011, ApJ, 737, 12
Leroy, A. K., Schinnerer, E., Hughes, A., et al. 2021, ApJS, 257, 43
Madden, S. C., Cormier, D., Hony, S., et al. 2020, A&A, 643, A141
Madden, S. C., Poglitsch, A., Geis, N., Stacey, G. J., & Townes, C. H. 1997, ApJ, 483, 200
McKee, C. F., & Ostriker, E. C. 2007, ARA&A, 45, 565
Narayanan, D., Krumholz, M. R., Ostriker, E. C., & Hernquist, L. 2012, MNRAS, 421, 3127
Pak, S., Jaffe, D. T., van Dishoeck, E. F., Johansson, L. E. B., & Booth, R. S. 1998, ApJ, 498, 735

Peñaloza, C. H., Clark, P. C., Glover, S. C. O., & Klessen, R. S. 2018, MNRAS, 475, 1508
Peñaloza, C. H., Clark, P. C., Glover, S. C. O., Shetty, R., & Klessen, R. S. 2017, MNRAS, 465, 2277
Pineda, J. E., Caselli, P., & Goodman, A. A. 2008, ApJ, 679, 481
Richings, A. J., & Schaye, J. 2016, MNRAS, 458, 270
Rubio, M., Elmegreen, B. G., Hunter, D. A., et al. 2015, Natur, 525, 218
Schöier, F. L., van der Tak, F. F. S., van Dishoeck, E. F., & Black, J. H. 2005, A&A, 432, 369
Schruba, A., Leroy, A. K., Kruijssen, J. M. D., et al. 2017, ApJ, 835, 278
Schruba, A., Leroy, A. K., Walter, F., et al. 2012, AJ, 143, 138
Seifried, D., Haid, S., Walch, S., Borchert, E. M. A., & Bisbas, T. G. 2020, MNRAS, 492, 1465
Seifried, D., Walch, S., Girichidis, P., et al. 2017, MNRAS, 472, 4797
Shetty, R., Glover, S. C., Dullemond, C. P., & Klessen, R. S. 2011a, MNRAS, 412, 1686
Shetty, R., Glover, S. C., Dullemond, C. P., et al. 2011b, MNRAS, 415, 3253
Shi, Y., Wang, J., Zhang, Z.-Y., et al. 2015, ApJL, 804, L11
Smith, R. J., Treß, R. G., Sormani, M. C., et al. 2020, MNRAS, 492, 1594
Springel, V. 2005, MNRAS, 364, 1105
Sternberg, A., & Dalgarno, A. 1995, ApJS, 99, 565
Tacconi, L. J., Genzel, R., & Sternberg, A. 2020, ARA&A, 58, 157
van Dishoeck, E. F., & Black, J. H. 1988, ApJ, 334, 771
Wernli, M., Valiron, P., Faure, A., et al. 2006, A&A, 446, 367
Wolfire, M. G., Hollenbach, D., & McKee, C. F. 2010, ApJ, 716, 1191